Available online at www.sciencedirect.com

SciVerse ScienceDirect

Procedia Engineering 00 (2012) 000–000

Procedia Engineering

www.elsevier.com/locate/procedia

5th BSME International Conference on Thermal Engineering

Numerical and Experimental Investigation of Winglet Plasma Actuators

A.N.M. Mominul Islam Mukut[a]*, Hiroshi Mizunuma[b], Obara Hiromichi[b], Takehiko Segawa[c]

[a]*Department of Mechanical Engineering, Dhaka University of Engineering & Technology (DUET), Gazipur-1700. Bangladesh*
[b] *Department of Mechanical Engineering,Tokyo Mectropolitan University, 1-1Minami-Osawa, Hachioji, Toky0 192-0397,*
[c] *National Institute of Advanced Industrial Science and Technology (AIST), Tsukuba, Japan*

Abstract

Plasma actuator has some advantages of simple mechanism, easy maintenance, having no moving parts, low cost and fast response compared with the other actuator as blow, suction or heating process. The surface Dielectric Barrier Discharge (DBD) plasma actuator is known to be effective for flow control process. This paper mainly investigated the winglet type DBD plasma actuators having exposed electrode on both sides in quiescent air that was investigated by means of particle image velocimetry. Numerical simulation has been carried out to clarify near electrode flow. High induced velocity has been found near the exposed electrode that was placed at leading edge. From two exposed electrodes on both sides of plasma actuator, two separate jet flows were induced after the winglet trailing edge and were unified to a single jet. The electrode location influenced the maximum velocity downstream. The longer distance between trailing edge and embedded electrode reduced the downstream unified velocity.

Keywords: dielectric barrier discharge plasma actuator, velocity profile, flow control, PIV, jet, CFD

Nomenclature

f_B	body force vector, N/m^3
U_x	x component of velocity, m/s
Greek symbols	
μ	viscosity, kg/m.s
ρ	density, kg/m^3

1. Introduction

Dielectric barrier discharges (DBD) has seen a tremendous growth in Aerodynamic flow control in the past years because of its demonstrated ability and potential applications. Some of them are active airfoil leading edge separation control [1,2], control of airfoil dynamic stall [3], bluff body flow control [4,5], boundary layer flow control [6,7], high-lift applications [8], and turbomachinery flow control [9,10] and so on. A simple plasma actuator is consists of two electrodes that are separated by a dielectric material. One of the electrode is typically exposed to the air. The other electrode is fully covered by the dielectric material. The electrodes are supplied with an AC voltage with enough magnitude which ionize the air over the covered electrode. Here the term ionized referred as plasma, that's why they are referred as Plasma Actuator. The word ''plasma'' was introduced into the physics literature by Langmuir [11] to denote an electrically neutral region of gas

* Corresponding author. Tel.: +8801913471401; fax: +88-02-9204710.
E-mail address: engrmukut@gmail.com

discharge. The ionized air, in the presence of the electric field produced by the electrode geometry produce a body force vector that acts on the ambient (neutrally charged) air. The body force is the mechanism for active aerodynamic control.

The plasma actuator is thin and controllable electrically. Until now, the actuators have been mounted on the wall surface. For example, a vortex generator is located on the wall surface and LEBU (Large Eddy Break Up) device is located with some distance from the wall surface. These devices are composed of thin plates which are requested to have simple structure and minimum sizes. Thus the applications are limited to passive flow control. On the other hand, the DBD plasma actuator has a function of the active control in spite of its simple structure. Thus if the combination of those passive control devices and the DBD plasma actuator is possible, it is expected to bring a new active method for the flow control. From this point of view, a plate-like plasma actuator located with a distance from the wall surface has been developed. In this paper three type of plasma actuators are numerically and experimentally evaluated to figure out their effectiveness so that they can be used as vortex generator to control flow separation.

2. Method

2.1. Experimental setup

Three types of Plasma Actuator (hereafter PA) namely: Leading edge type (hereafter L type) PA, Middle edge type (hereafter M type) PA and Trailing edge type (hereafter T type) PA have been used in experiment. All of these PA have two exposed electrode on both sides with common embedded electrode; convectional two PA have been glued together to make our desired PA. The width and chord length of mini-plate wing were 96 mm and 19.6 mm respectively. The electric wind was generated in the absence of external flow by the plasma actuator. Exposed and grounded electrodes were separated by a Kapton thin wing plate. Detailed dimension (all in mm) have been shown in figure 1. The induced flow was compared as a function of the distance from the leading edge to the actuator position. Due to use of two exposed electrodes plasma was created on both sides of actuator surfaces. All experiments were carried out with a frequency of 5 kHz and the corresponding applied voltage were 2.5kV, 3kV, 3.5kV and 4kV respectively. All experiments were carried out in absence of external air flow.

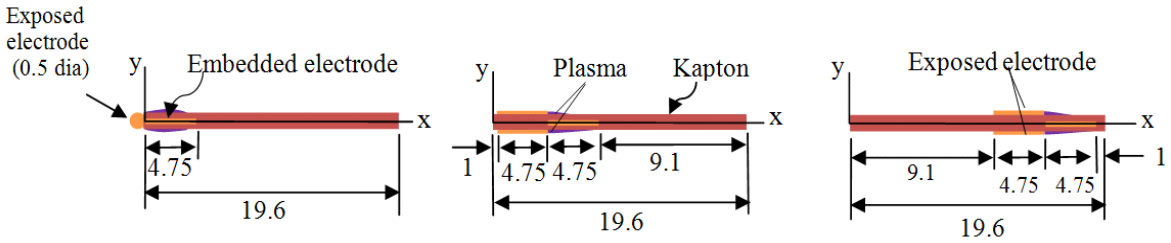

Fig.1. Plasma actuator geometry (all dimension in mm)

Particle image velocimetry (PIV) was employed to quantify the behavior of the flow field during testing at AIST Tsukuba [12]. The laser is a 25 mJ/pulse, double-pulse Nd-YAG laser (New Wave Research Co. Ltd., MiniLase II: 20 Hz).

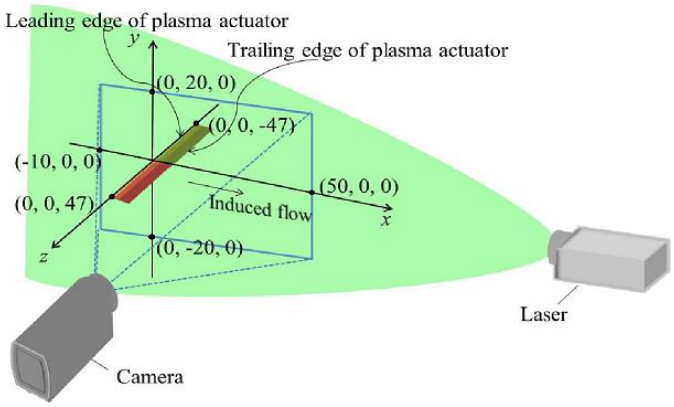

Fig.2. PIV setup

A horizontal laser sheet would strike at the midpoint of the plasma actuator from downstream, so that only suction side was in shadow. This enabled us to measure a two dimensional cross-section of the flow field around the airfoil. The schematic diagram of PIV experiment is presented in figure 2.

2.2. Simulation

Due to use of two exposed electrodes, plasma was created on both side of embedded electrode. In PIV measurement, near electrode flow was not so clear due to plasma and laser light reflection, that's why numerical simulation has been carried out to investigate flow at near electrode region.

Modeling and numerical simulation have been performed based on Suzen et al. [13]. Main concept is same but difference in PA size and shape. Embedded type electrode was used by Suzen but in this present research mini plate wing type PA has been investigated, this is due to the aim of combining active and passive flow control device.

The governing equation is 2D unsteady Navier-Stocks equation which is given below:

$$\frac{\partial u}{\partial x}+\frac{\partial u}{\partial y}=0 \qquad (1)$$

$$\frac{DU}{Dt}=-\frac{1}{\rho}\nabla p+\mu\nabla^2 U+\overrightarrow{f_B} \qquad (2)$$

Finite volume method has been applied in simulation using above mentioned equations. PHOENICS 2009 solver which is developed by CHAM, UK has been used for simulation. Simulation is consist of two steps: at first the electrical potential, the particle charge density and EHD forces were calculated, secondly using those values induced flow was calculated. Unsteady flow was considered in simulation and the average was calculated to compare those with the time averaged result of PIV.

3. Result and discussion

Due to pair of exposed electrodes, two induced flow were produced that were unified downstream of winglet. In this paper, experimental PA mini plate wing thickness was 0.75mm and due to both side plasma huge reflection of light, image resolution near electrodes was not good. Hence numerical simulation has been carried out to figure out near electrode flow. Also due to limitation of image resolution in PIV experiment two separate induced flows near the winglet was not identified but in simulation two separate induced flows have been identified clearly.

Downstream unification of two separate induced flows was clear and well match in both experiment and simulation, to clarify it center jet velocity has been shown in figure 3. As near electrode flow was not clear in experiment hence comparison of experimental and simulated velocity profile have been figure out at x=30mm from origin which is downstream of winglet and presented in figure 4 for 4kV applied voltage only. This figures also made a comparison with Jamey et al [14] of whose plasma actuator dimension is nearly same as present research, measuring location is also same i.e. at 30mm downstream but only difference in applied voltage (5kV), square wave frequency (4.5 kHz) and single exposed electrode. Induced flow increased with applied voltage with all electrode arrangements. Simulation and experimental velocity profiles were reasonable except peak velocity area due to PIV image resolution. In simulation mesh grid is too smaller than experimental measuring grid as a result two peaks clearly appeared in simulation.

Simulated and experimental velocity profile of each type PA for 4kV applied voltage were plotted at figure 5 and compared with S. Okochi et al [15]. Higher induced flow have been found in Okochi's research as he measured velocity near electrode region where as in this paper velocity measured 30mm downstream from origin. The velocity increases with the voltage because the electric field also increases and ions undergo higher Columbian forces [16].

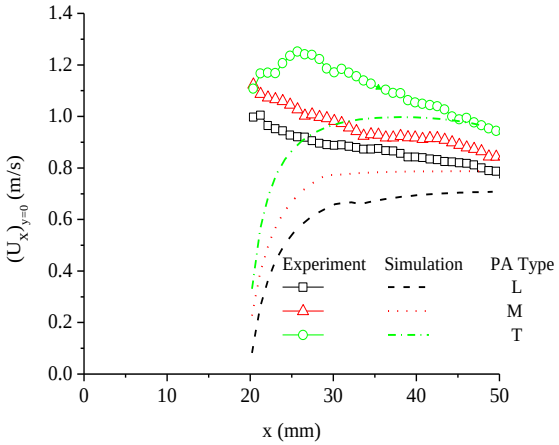

Fig. 3. Center jet velocity variation along x axis-4kV L-M-T type PA

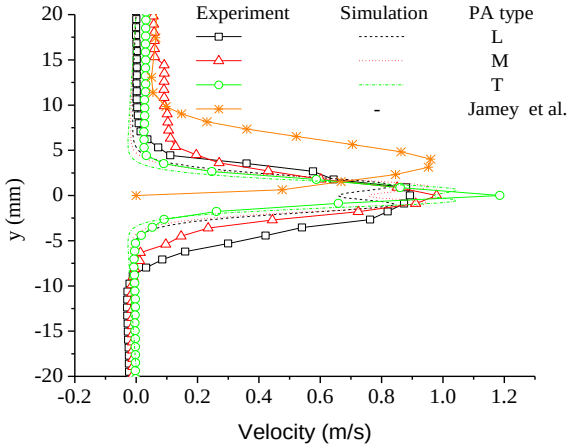

Fig. 4. Velocity profile-4kV applied voltage

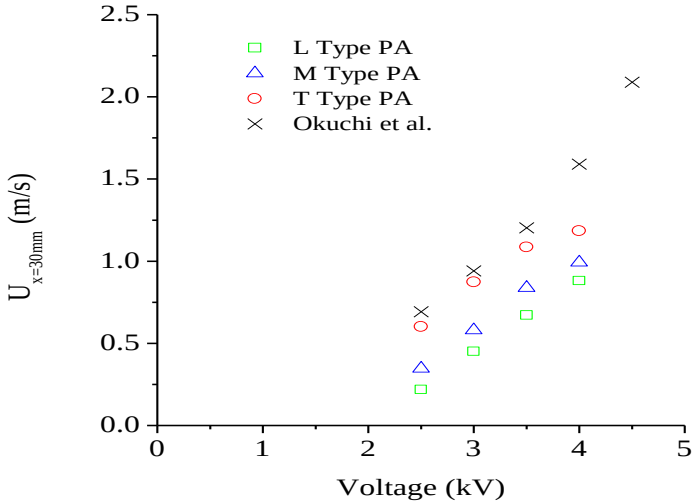

Fig. 5. Change of induced velocity (at x=30mm) with applied voltage

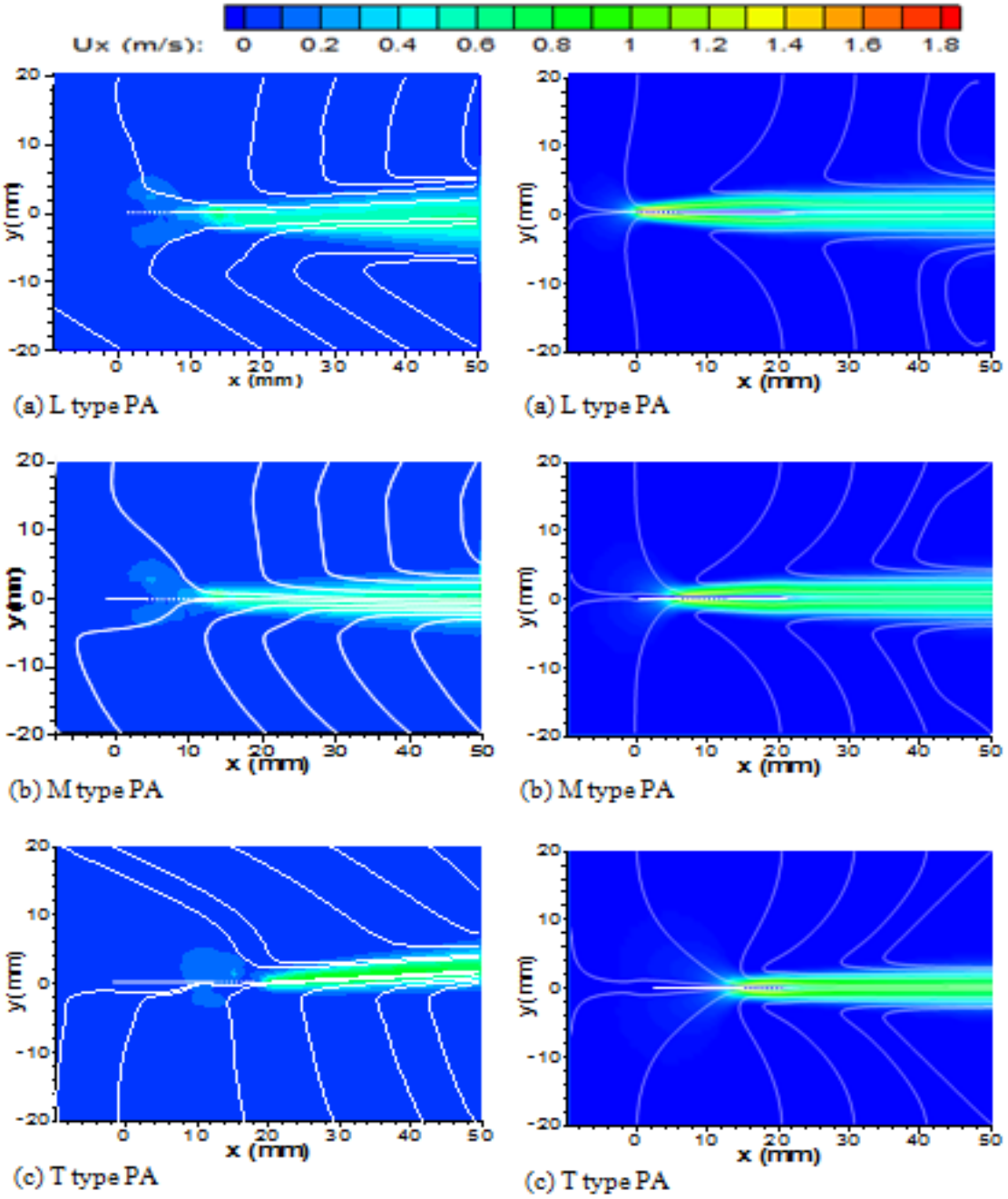

Fig.6(a) PIV measurement for streamlines and contour plot of U_x (3kV) -dotted line indicates corresponding embedded electrode location]

Fig. 6(b) Numerical simulation for streamlines and contour plot of U_x (3kV)- [dotted line indicates corresponding embedded electrode location]

Experimental and simulation contour and streamline plot have been represented in figure 6. Both experiment and simulation indicate wider jet width like L>M>T type PA. This is because the electrode arrangement on mini wing plate. When exposed electrode near leading edge then gap between exposed electrode and wing end is longer but when exposed electrode nearer to trailing edge this gap became

shorter. As a result T type PA has shorter trailing end gap and two unified flow faced small friction during flowing over this small gap which results higher unified flow than M and L type PA as these two types of PA have longer gap than T type.

Behavior of near electrode flow has been investigated easily from simulation. M and T type PA have same shape of electrode except location over plate, gave same trend of induced flow but M type provides lower induced flow at trailing end than T type PA.

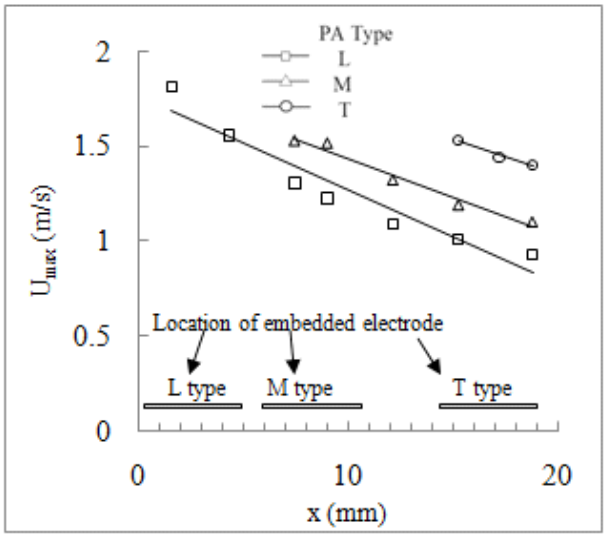

Fig.7, Trend of flow reduction over wing [4kV applied voltage]

On the other hand, L type PA gives maximum induced flow than M and T type PA but at downstream unification gave lowest flow than other two. Trend of flow reduction over embedded electrode has been shown in figure 7 based on peak velocity at each x locations. The reason is the end gap between the embedded electrode and trailing end of wing. Higher the end gap increase frictional loss which reduces downstream flow. In all three types of PA, maximum induced flow has been found at 0.44mm above (both side) of actuator surface. Along this y location, percentage of flow reduction has been calculated from velocity changes along x axis and presented at table 1.

Table 1. Calculation of flow reduction over wing

Type of Actuator	Max. induced flow velocity (m/s)	Velocity at the end of wing plate (m/s)	% of flow reduction
L type PA	1.81	0.35	80.51%
M type PA	1.53	0.599	60.74%
T type PA	1.53	1.2	21.597%

It is found that increase in distance between embedded electrodes and tailing end of wing, decrease in induced flow at the end of tailing edge which also give lower magnitude of unified flow at downstream

4. Conclusion

In this paper, experimental analysis and numerical modelling have been performed to evaluate special design plasma actuator. Effect of end gap and shape of exposed electrodes have been investigated. From the

above mentioned analyses it is clear that lower the end gap results in lower frictional loss which gave higher unified induced flow, as a result T type PA gave higher unified induced velocity at downstream. Shape of exposed electrode has a great role on near electrode flow. Only L type PA has wire type exposed electrode, from simulation it is found that this type of PA provides maximum induced flow over embedded electrode than that of M and T type PA as shape of exposed electrode is different. Both M and T type PA have same shape of exposed electrode but only difference is in electrode position on mini-plate wing and both of these PA gave same magnitude of induced flow. So, it is clear that shape of exposed electrode has a great influence on induced flow.

References

[1] Post, M. L., and Corke, T. C., 2004, "Separation Control on a High Angle of Attack Airfoil Using Plasma Actuators," AIAA Journal, Vol. 42, No. 11, pp. 2177–2184.

[2] Benard, N., Braud, P., and Jolibois, J.2008,"Airflow Reattachment Along a NACA 0015 Airfoil by Surface SDBD Actuator-Time Resolved PIV Investigation," AIAA Paper 2008-4202.

[3] Post, M. L., and Corke, T. C.,2006, "Separation Control Using Plasma Actuators—Dynamic Stall Vortex Control on an Oscillating Airfoil," AIAA Journal, Vol. 44, No. 12, pp. 3125–3135.

[4] Do, H., Kim, W., Mungal, M. O., and Cappelli, M. A., 2007, "Bluff Body Flow Separation Control Using Surface Dielectric Barrier Discharges," AIAA Paper 2007-939.

[5] Thomas, F. O., Kozlov, A., and Corke, T. C., 2008, "Plasma Actuators for Cylinder Flow Control and Noise Reduction", AIAA Journal, Vol. 46, No. 8, pp. 1921–1931

[6] Schatzman, D., and Thomas, F. O., 2008, "Turbulent Boundary Layer Separation Control Using Plasma Actuators,"AIAA Paper 2008-4199

[7] Baughn, J.W., Porter, C., Peterson, B.L., McLaughlin, T.E., Enloe, C.L., Font, G. I., and Baird, C. 2006,"Momentum Transfer for an Aerodynamic Plasma Actuator with an Imposed Boundary Layer," AIAA Paper 2006-168.

[8] Corke, T. C., He, C., and Patel, M., 2004, "Plasma Flaps and Slats: An Application of Weakly-Ionized Plasma Actuators," AIAA Paper 2004-2127.

[9] Huang, J., Corke, T. C., and Thomas, F. O., 2006, "Plasma Actuators for Separation Control of Low-Pressure Turbine Blades," AIAA Journal, Vol. 44, No. 1 pp. 51–57.

[10] Van Ness, D. K., II, Corke, T. C., and Morris, S. C., 2006, "Turbine Tip Clearance Flow Control Using Plasma Actuators," AIAA Paper 2006-0021.

[11] Langmuir I (1926) Proc Nat Acad Sci 14:627

[12] Seth Walker, Takehiko Segawa, Timothy Jukes, Hirohide Furutani, Norihiko Iki, Shinya Takekawa. 2012, "Active Control Of Flow Separation Over a NACA 0024 Airfoil By DBD Plasma Actuator And FBG Sensor", Journal of Fluid Science and Technology, Volume 7, Issue 1, pp. 39-52

[13] Y. B. Suzen, P.G. Huang, J.D. Jacob and D.E. Ashpis, "Numerical simulation of plasma based flow control applications", 35th Fluid Dynamics Conference and Exhibit, AIAA-4633

[14] Jamey D. Jacob, Karthik Ramakumar, Rich Anthony and Richard B. Rivir, 2005, "Control of laminar and turbulent shear flows using plasma actuators.", 4th International Symposium on Turbulence and Shear Flow Phenomena, Williamsburg, VA June 2 7–29.

[15] S. Okochi, N. Kasagi, Y. Suzuki, S. Ito, "Development of micro plasma actuator for active flow control", 7th World Conference on Experimental Heat Transfer, Fluid Mechanics and Thermodynamics.

[16] M. Forte, J. Jolibois, F. Baudoin, E. Moreau, G. Touchard, M. Cazalens, "Optimization of a dielectric barrier discharge actuator by stationary and non-stationary measurements of the induced flow velocity: application to airflow control", Exp Fluids 43:917–928

Available online at www.sciencedirect.com

SciVerse ScienceDirect

Procedia Engineering 00 (2012) 000–000

Procedia Engineering

www.elsevier.com/locate/procedia

5th BSME International Conference on Thermal Engineering

Suppression of Fluid Forces on Two Staggered Cylinders

Md. Mahbub Alam[1*] and Y. Zhou[1,2]

[1]Shenzhen Graduate School, Harbin Institute of Technology, Shenzhen, China
[2]Mechanical Engineering Department, The Hong Kong Polytechnic University, Hong Kong.

Abstract

An investigation is conducted to suppress flow-induced forces on two identical cylinders (diameter D = 49 mm) at stagger angle $\alpha = 0^{\circ} \sim 180^{\circ}$ and gap spacing ratio $T/D = 0.1 \sim 5$, where T is the gap width between the cylinders. In order to suppress fluid forces, two tripwires, each of 5 mm, were attached on each cylinder at azimuthal angle $\beta = \pm 30^{\circ}$. Time-mean drag (C_D) and fluctuating drag (C_{Df}) and lift (C_{Lf}) on two tripped cylinders were measured and compared with those on plain cylinders. Flow visualization test was also conducted to observe flow structures around the cylinders. C_D, C_{Df} and C_{Lf} all for the plain cylinders are strong function of α and T/D due to six different interaction mechanisms. On the other hand, the tripped cylinders interfere weakly each other, resulting in insignificant variation in forces with α and T/D. Tripwires suppress forces on the cylinders remarkably.

Keywords: Two cylinders, drag, lift, trip wires, supression, interaction

Nomenclature

u_θ	velocity in the direction of (m/s)
A	radius of (m)
B	position of
C	further nomenclature continues down the page inside the text box
Greek symbols	
γ	stoichiometric coefficient
δ	boundary layer thicknesses(m)
Subscripts	
r	radial coordinate

* Corresponding author: Tel: +8675526623472
Email: alamm28@yahoo.com; alam@hitsz.edu.cn

1. Introduction

The alternate shedding of vortices in the near wake leads to fluctuating forces on the structures and may cause structural vibrations, acoustic noise, or resonance, which in some cases can trigger failure. In a real life architectural environment, most buildings and structures are in close proximity of each other, such as chimney stacks, tube bundles in heat exchangers, overhead power-line bundles, bridge piers, stays, masts, chemical-reaction towers, offshore platforms and adjacent skyscrapers. Aerodynamics of two closely separated structures is of both fundamental and practical significance. Two cylinders are considered as the basic model to understand the physics of flow around multiple structures. Fluid forces, Strouhal numbers (*St*) and flow structures are the major factors considered in the design of multiple slender structures subjected to cross flow. The flow around two cylinders is apparently more complicated than that around a single one.

Based on the interference effect between two cylinders, Zdravkovich [1] divided the whole region of possible arrangements of two cylinders into four; (i) the proximity interference region, where the flow around one cylinder affects the other; (ii) wake interference region, the near-wake flow of the upstream cylinder is unaffected by the downstream one; however, the downstream one is significantly affected by the upstream cylinder; (iii) the proximity and wake interference region includes the combination of the proximity and wake interferences; (iv) the no interference region, where the wake of one cylinder does not affect the other. This classification is useful from the engineering design point of view, though providing little information on the flow structure around the cylinders.

Time-averaged drag and lift forces acting on two staggered cylinders have been examined in literatures (e.g., [2, 3]). However, data in the literatures are mostly concerned with the downstream cylinder. A review of literature indicated that due to interference between the cylinders, fluctuating lift and drag forces on two staggered circular cylinders are intensified depending on *T/D* and α, where *T* is the gap spacing between the cylinders, *D* is the cylinder diameter and α is the stagger angle between the free-stream flow and the line connecting the centers of the cylinders. No method has however been established to suppress the intensified forces. Use of tripwires to control boundary layer on a cylinder is interesting and effective [4]. Alam et al. [5] used tripwires as control objects to suppress forces on two cylinders in tandem and side-by-side configurations.

The objectives of this study were to (i) find the possible interaction mechanisms between two plain cylinders and (ii) reduce flow-induced forces on and inference between the cylinders using tripwires, where *T* is the gap width between the cylinders, *D* is the diameter of a cylinder and α is the stagger angle. Measurements were conducted at $\alpha = 0^{\circ} \sim 180^{\circ}$, $T/D = 0.1 \sim 5.0$. The linkage between force and flow structure and the interactions between the cylinders are discussed in details.

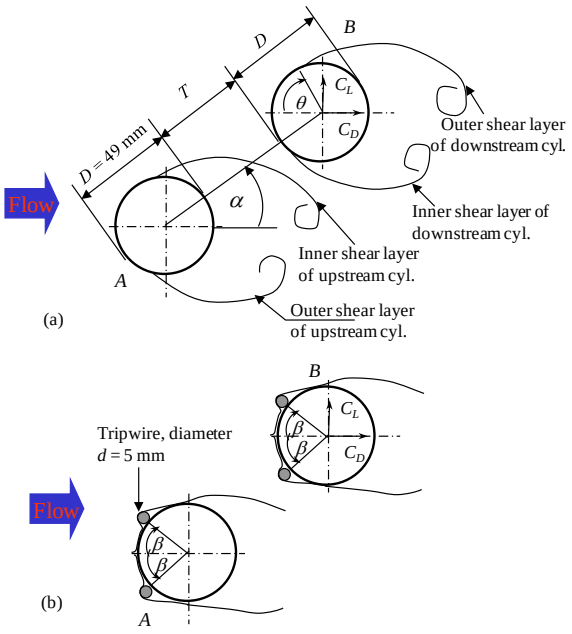

Fig. 1. Definitions of symbols and arrangement of cylinder (a) without tripwires, (b) with tripwires.

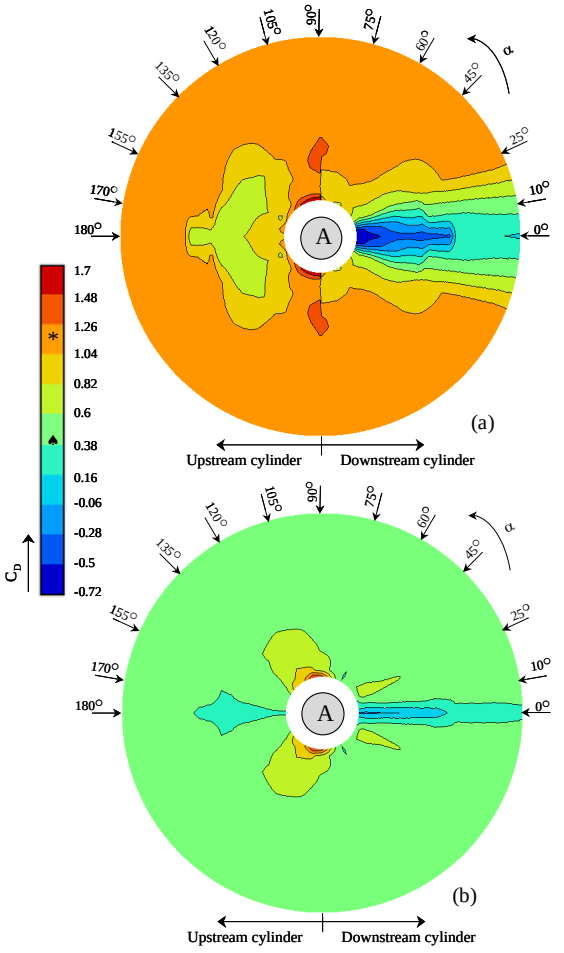

Fig. 2. Contour plot of time averaged drag coefficient, C_D: (a) plain cylinders, (b) tripped cylinders. '*' and '♠' denotes C_D values of a single cylinder plain and tripped, respectively.

2. Experimental detail

Measurements were done in a closed-circuit wind tunnel with a test section of 1.20×0.30 m at the fluid mechanics laboratory of Kitami Institute of Technology, Japan. The Reynolds number (*Re*) based on the diameter of a single cylinder was 5.52×10^4 and the turbulent intensity was 0.5%. C_D, C_{Df} and C_{Lf} were measured using two load cells installed inside a circular cylinder of diameter D = 49 mm. See Alam et al. [6] for details of the load cell. Two tripwires, each of 5 mm were placed at azimuthal angle $\beta = \pm30^\circ$ measured from front stagnation point. The β was decided based on optimum suppression of forces on a single cylinder [5]. Experiments were performed at $\alpha = 0^\circ$, 10°, 25°, 45°, 60°, 75°, 90°, 105°, 120°, 135°, 155°, 170°, and 180°, for $T/D = 0.1 \sim 5$. Flow visualization was carried out at Re = 350 in a water channel with a 250 mm × 350 mm working section and 1.5 m long. In the flow visualization test, two circular cylinders with identical diameter of 20 mm were used.

3. Results and discussion

3.1. Fluid forces on the cylinders

Contours of C_D, C_{Df} and C_{Lf} on a T/D-α plane are shown in Figs. 2-4 for the cases of the plain and tripped cylinders. Here tripped cylinders mean cylinders with tripwires. In the scale bars, the color or the range marked by '*' and '♠' indicates the value of a single isolated plain and tripped cylinders, respectively. For the purpose of simplicity, the result can be described with reference to Fig. 1, in which the cylinder *A* is tentatively assumed to be fixed, and thus the two parameters T/D and α suffice to determine the arrangement of the two cylinders. It may be noted that the cylinder *B* is the downstream cylinder for $-90^\circ < \alpha < 90^\circ$ and it becomes the upstream cylinder for $90^\circ < \alpha < -90^\circ$, i.e., the left and right sides of a contour map show the values of coefficient of the upstream and downstream cylinders, respectively. At the peripheries of the inner and outer circles, the values of T/D are 0 and T/D = 5.0, respectively. Note that the values of C_D, C_{Df}, and C_{Lf} of a single plain cylinder are 1.12, 0.14, and 0.48, respectively. Repulsive (upward directed) C_L is considered as positive (Fig. 1).

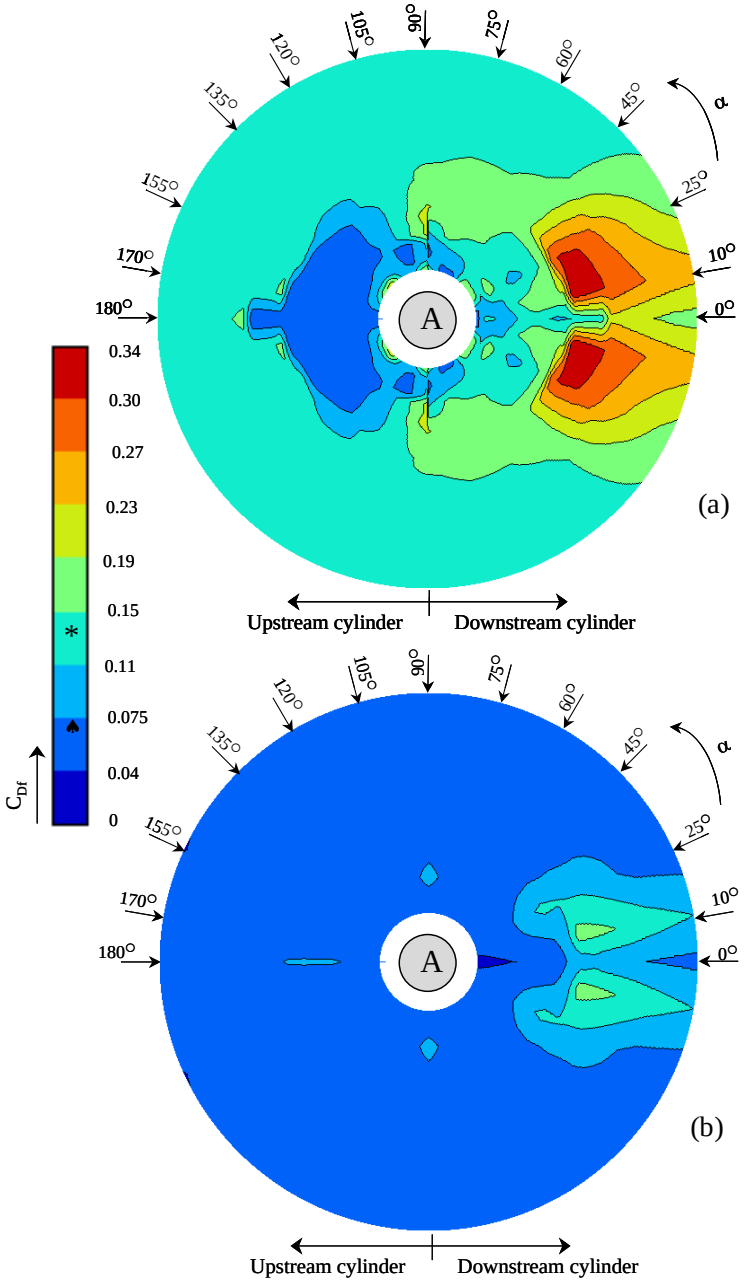

Fig. 3. Contour plot of fluctuating drag coefficient, C_{Df}: (a) plain cylinders, (b) tripped cylinders. '*' and '♠' denotes C_{Df} values of a single cylinder plain and tripped, respectively.

The contour maps show that C_D, C_{Df} and C_{Lf} of the plain cylinders briskly vary with change in T/D and α (Figs. 2a, 3a, 4a). However, those of the tripped cylinders vary rather mildly. The observation suggests that interference between the plain cylinders is much strong but that between the tripped cylinders is weak. For the case of plain cylinders, it is seen that the upstream cylinder experiences somewhat lower C_D at $\alpha = -120^\circ \sim 120^\circ$, $T/D < 3.0$ than a single isolated cylinder (Fig. 2a). The downstream cylinder experiences highly negative C_D at $\alpha = -10^\circ \sim 10^\circ$, $T/D < 3.0$, with a maximum negative value of -

0.72 when it is in contact with the upstream cylinder at $\alpha = 0^\circ$. Maximum C_D acts on the two cylinders when they are arranged in side-by-side with $T/D = 1.2 \sim 2.0$ in which an enhanced antiphase vortex shedding occurs from the cylinders. A significantly higher C_D acts on the upstream cylinder at $\pm 90^\circ < \alpha < \pm 120^\circ$, $T/D < 0.2$. For the case of tripped cylinders, a significant reduction in C_D is observed over the whole region except the region bounded by $T/D < 0.2$, $\alpha = 90^\circ \sim 105^\circ$ where color is still red. In this region, however, C_D can be reduced by changing the positions of the outer tripping wires toward the forward. Value of C_D on the most of the region is 1.04 ~ 1.26 (Fig. 2a) which have been suppressed to 0.38~0.6 by using tripping wires (Fig. 2b). On average, the suppression in C_D is about 58%. Figure 2(b) indicates that mutual interference between the cylinders is greatly weakened when tripping wires are used on the cylinders, which was an objective of this study.

For the case of plain cylinders, significantly higher magnitudes of C_{Lf} and C_{Df} act on the downstream cylinder at $\alpha = -35^\circ \sim 35^\circ$, $T/D > 2.5$ (Figs. 3a, 4a). C_{Lf} and C_{Df} on the upstream cylinder become extremely small for $\alpha = -120^\circ \sim 120^\circ$, $T/D < 3.0$ and on both cylinders in the vicinity of side-by-side arrangement at small T/D. In the first region, they become very small because formation of fully developed Karman vortex behind the upstream cylinder is retarded by the presence of the downstream cylinder [6]. In the second region, the gap flow between the cylinders acts as a base bleed, propelling the rolling positions of the outer shear layers downstream, causing small C_{Lf} and C_{Df}.

C_{Df} of the tripped cylinders is suppressed to very small value for the whole region, compared that of the plain cylinders. The value of C_{Df} in the region $\alpha = 10^\circ \sim 25^\circ$, $T/D = 2.5 \sim 3.5$ is maximum 0.30 ~ 0.34 for the plain cylinders and reduces to 0.15~0.19 when tripping wires are used. Here also mutual interference effect between the tripped cylinders is very small. A dramatic decrease in C_{Lf} is self-evident for tripped cylinders compared to plain cylinders (Fig. 4b). C_{Lf} in the red region (maximum values of C_{Lf}) of the plain cylinders has been reduced to significantly small value by the tripping wires on the cylinders. Thus use of tripping wires on two cylinders is an effective means for suppressing interference between and forces acting on two cylinders in any arrangements.

3.2. Interaction mechanisms

A single cylinder in cross-flow in general generates boundary layers, shear layers, alternating vortices and wake. When two cylinders are in close proximity, boundary layers, shear layer, vortex and wake are therefore four physical interacting parameters. A scrupulous observation of flow structures

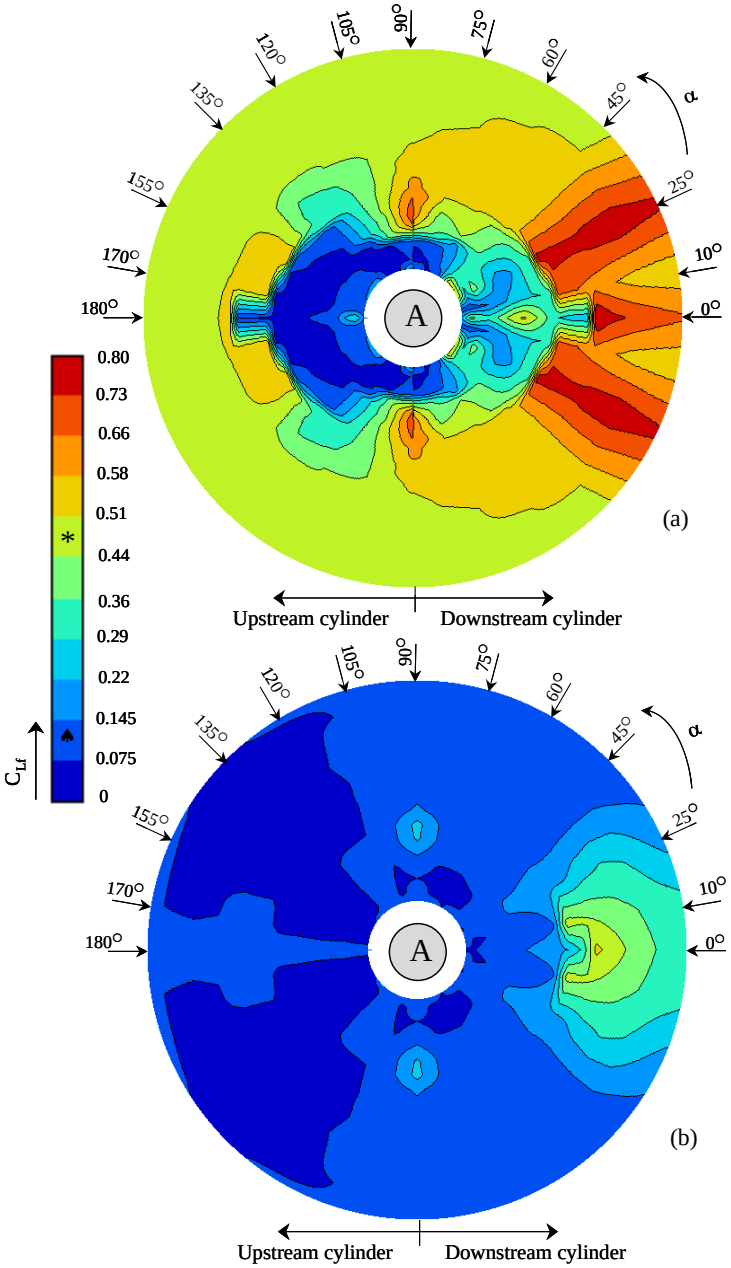

Fig. 4. Contour plot of fluctuating lift coefficient, C_{Lf}: (a) plain cylinders, (b) tripped cylinders. '*' and '♠' denotes C_{Lf} values of a single cylinder plain and tripped, respectively.

reveals the interactions of the six types. They are interaction between (i) boundary-layer and cylinder, (ii) shear-layer/wake and cylinder, (iii) shear layer and shear layer, (iv) vortex and cylinder, (v) vortex and shear layer, and (vi) vortex and vortex. Their regimes are given in Fig. 5. The details of the interactions are given as follows.

Boundary-layer and cylinder interaction: this interaction occurs when T/D is small, T/D < 0.3 - 0.6 depending on α. Interacting with the other cylinder, boundary-layer of a cylinder may form separation bubbles, delay to separate, reattach, etc. See Fig. 5c. The interaction therefore intensifies C_D and C_L but weakens C_{Df} and C_{Lf}. The two cylinders being very close behave like a combined cylinder.

Shear-layer/wake and cylinder interaction: this happens when shear layer(s) from one cylinder interacts on the other cylinder surface by reattaching, impinging, forming separation bubble, etc. (Fig. 5d, e). Naturally, one of the cylinders is completely (Fig. 5d) or partially (Fig. 5e) submerged in the wake of the other, hence it can also be termed as wake and cylinder interaction. The shear layer interacted by the cylinder loses its strength to shed alternating Karman vortex, hence forces wane significantly. Being completely submerged in the wake of the other, the cylinder acting as a stabilizer suppresses the flow unsteadiness between the cylinders. The interaction occurs when two cylinders are nearly in-line, $|\alpha| \approx 0^{\circ} \sim 20^{\circ}$, 0.3 < T/D < 2.3 - 3.

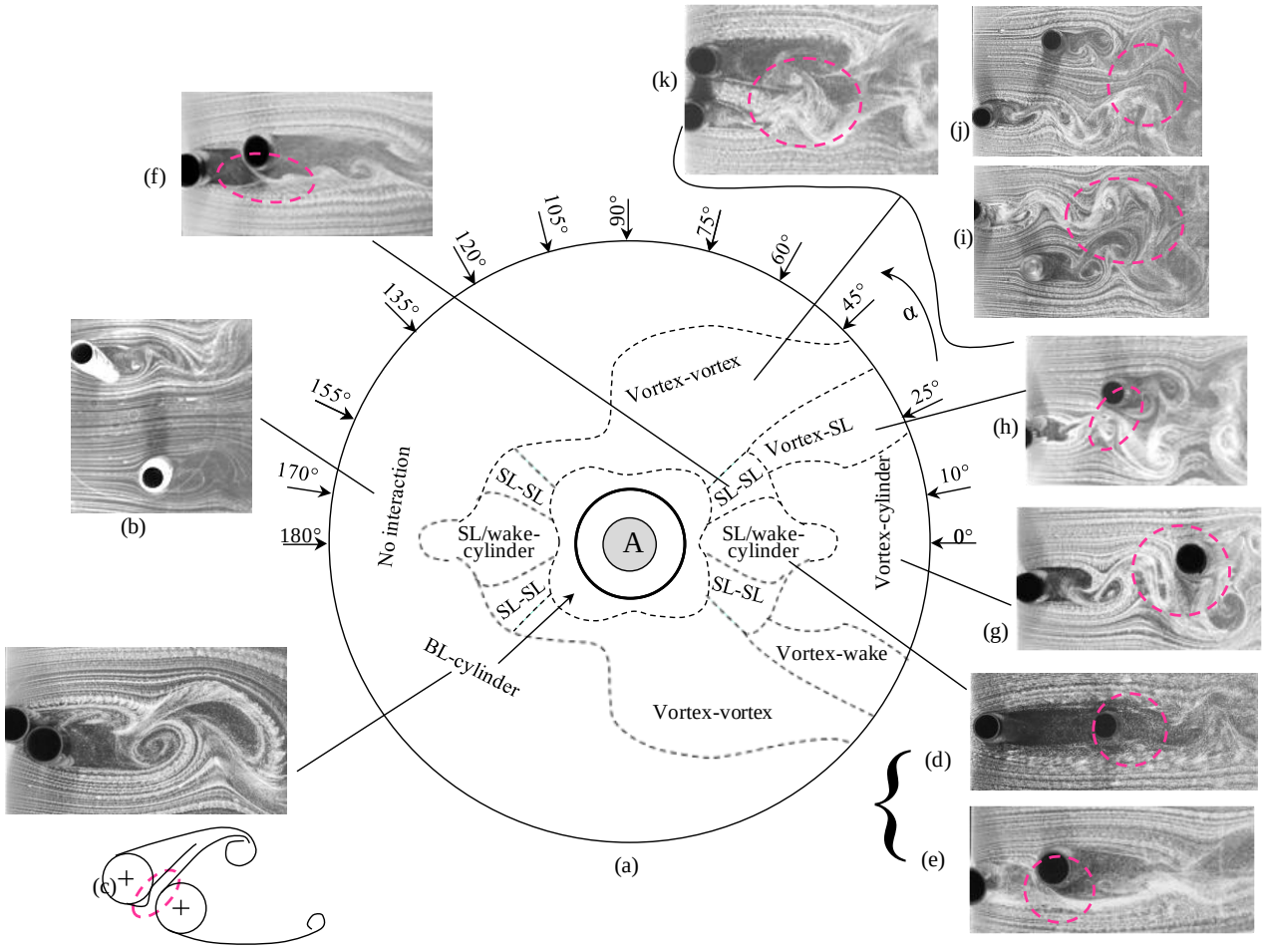

Fig. 5. Interaction regimes in T/D - α plane. SL : shear layer, BL : boundary layer.

Shear layer and shear layer interaction: here the shear layer(s) of a cylinder directly interacts with that of the other. The interaction causes intermittent interlock-in of the shear layers, hence generates vortices at more than one frequency (Fig. 5f), and reduces forces on the cylinders. Since α of this interaction regime is higher than that of shear layer/wake and cylinder interaction regime, generation of two shear layers through the gap is possible. The two shear layers interact with themselves and the outer-shear layers.

Vortex and cylinder interaction: when T/D is greater than the critical spacing of two nearly in-line cylinders, the shear layers of the upstream cylinder cannot reach the downstream cylinder, hence roll between the cylinders, forming

alternate vortices. Thus the alternate vortices from the upstream cylinder strike on the downstream cylinder and embrace the side surface during passing on the cylinder (Fig. 5g). This interaction is generally very strong, intensifying C_{Df} significantly. Gursul and Rockwell [7] investigated the interaction of oncoming two rows of vortices on an elliptical leading edge and observed very high fluctuating pressure on the surface where vortices reached.

Vortex and shear-layer interaction: for a larger α, the downstream cylinder becomes offset from the inner row of vortices from the upstream cylinder, hence the vortices cannot interact with the downstream cylinder, but can interact with the inner-shear layer. Interacting with the shear layer while it is growing, the vortices force the shear layer to form a synchronized coupled vortex (Fig. 5h). This interaction renders a very high C_{Lf}, as alternate interaction between vortex and shear layer intervenes.

Vortex and vortex interaction: for a further increase in α, the transverse distance between the cylinders becomes large, hence each cylinder forms a separate wake immediately behind them. The vortices on the two inner rows interact with each other and combines the two wakes into a wider one (Fig. 5i, j, k), which results in a slightly higher C_D, C_{Df} and C_{Lf}.

For the case of tripped cylinders, flow around the cylinders over the entire region is almost the same except $-25^\circ < \alpha < 25^\circ$. The actions of all the possible interactions are reduced. Mutual interference effect between the cylinders is reduced significantly; as a result, C_D, C_{Df} and C_{Lf} are almost insensitive to T/D and α.

As sketched in Fig. 1(b), the flow structure on the tripped cylinders has the following features: (i) shear layer separating from the tripwires reattach on the cylinder surface, (ii) the eventual separation is postponed, (iii) wake narrows, and (iv) vortex shedding is almost suppressed from the cylinders. A cylinder with these features do not interfere the other. However, for $\alpha < 25^\circ$, the downstream cylinder is submerged in the wake of the upstream cylinder, hence interfered weakly.

4. Conclusions

The results can be summarized as follows.

Fluctuating drag coefficient (C_{Df}) and Fluctuating lift coefficient (C_{Lf}) on the downstream cylinder are extensively high in two island-like regions $\alpha = \pm (10^\circ \sim 30^\circ)$, $T/D = 2.5 \sim 5$, where the inner shear layer of the downstream cylinder sheds vortices in synchronization with the convective inner vortices from the upstream cylinder, generating a coupled vortex. Tripping wires suppress C_{Df}, and C_{Lf} by about 55% and 70%, respectively in these regions.

While the plain cylinders each other intervene extensively, tripped cylinders do not; hence C_{Df} and C_{Lf} are almost insensitive to T/D and α. Compared to the plain cylinders, the tripped cylinders eperience smaller forces in the entire T/D and α ranges examined.

Six different interaction mechanisms between the cylinders were observed: boundary-layer and cylinder interaction, shear-layer/wake and cylinder interaction, shear layer and shear layer interaction, vortex and cylinder interaction, vortex and shear-layer interaction, and vortex and vortex interaction. Each of them had different influences on the induced forces. Both shear-layer/wake and cylinder, and boundary-layer and cylinder interactions weaken C_{Df}, C_{Lf} and flow unsteadiness. While the former interaction stabilizes the wake or shear layers, the latter one forms a separation bubble, delays boundary layer separation, or causes reattachment. The separation bubble formation results in maximum repulsive C_L of +0.86 at $|\alpha| = 135^\circ$, $T/D = 0.1 \sim 0.2$. Maximum C_D of 1.75 acts on the cylinders in the regime of $|\alpha| = 90^\circ$, $T/D = 2.2 \sim 2.6$ caused by a strong vortex and vortex interaction, which is about 1.56 times the single cylinder value.

References

[1] Zdravkovich MM. The effects of interference between circular cylinders in cross flow. J Fluids and Structures 1987; 1: 239-261.

[2] Zdravkovich MM. Pridden DL. Interference between two circular cylinders; series of unexpected discontinuities. J Industrial Aerodynamics 1977;. 2: 255-270.

[3] Price,SJ, Paidoussis MP. The aerodynamic forces acting on groups of two and three circular cylinders when subject to a cross-flow. J Wind Engineering and Industrial Aerodynamics 1984; 17: 329-347.

[4] Nebres J, Batill S. Flow about a circular cylinder with single large-scale surface perturbation. Exp. in Fluids 1993; 15: 369-379.

[5] Alam MM, Sakamoto H, Moriya M. Reduction of fluid forces acting on a single circular cylinder and two circular cylinders by using tripping rods. J Fluids and Structures 2003;18: 347-366.

[6] Alam MM, Sakamoto H, Zhou Y. Determination of flow configurations and fluid forces acting on fwo staggered cylinders of equal diameter in cross-flow. Journal of Fluids and Structures 2005; 21: 363-394.

[7] Gursul I, Rockwell D. Vortex-street impinging upon an elliptical leading edge. J Fluid Mechanics. 1990; 211, 211–242.

Available online at www.sciencedirect.com

SciVerse ScienceDirect

Procedia Engineering 00 (2012) 000–000

Procedia Engineering

www.elsevier.com/locate/procedia

5th BSME International Conference on Thermal Engineering

Transient Heat and Fluid Flow through a Rotating Curved Rectangular Duct: The Case of Positive and Negative Rotation

Rabindra Nath Mondal[a]* Md. Zohurul Islam[b] and Md. Saidul Islam[b]

[a] *Department. of Mathematics, Faculty of Science, Jagannath University, Dhaka-1000, Bangladesh*
[b] *Mathematics Discipline; Science, Engineering and Technology School, Khulna University, Khulna-9208, Bangladesh*
Email: rnmondal71@yahoo.com

Abstract

A comprehensive numerical study is presented for the fully developed two-dimensional thermal flow of viscous incompressible fluid through a rotating curved rectangular duct of constant curvature $\delta = 0.1$. Numerical calculations are carried out by using a spectral method, and covering a wide range of the Taylor number $-1000 \le Tr \le 3000$ and the Dean number $100 \le Dn \le 1000$ for the Grashof number $Gr = 100$. The outer wall of the duct is heated while the inner wall cooled. Flow characteristics are investigated for two cases of the duct rotation, *Case I*: Positive rotation and *Case II*: Negative rotation. For positive rotation, we investigate the unsteady flow characteristics for the Taylor number $0 \le Tr \le 3000$ and it is found that the unsteady flow undergoes in the scenario '*Chaotic* $\rightarrow$ *multi-periodic* $\rightarrow$ *periodic* $\rightarrow$ *steady-state'*, if *Tr* is increased in the positive direction. For negative rotation, however, we investigate the unsteady flow behavior for $-1000 \le Tr \le -100$, and it is found that the unsteady flow undergoes through various flow instabilities, if *Tr* is increased in the negative direction. Contours of secondary flow patterns and temperature profiles are also obtained at several values of *Tr*, and it is found that there exist two- and multi-vortex solutions if the duct rotation is involved in both the directions.

Keywords: Curved rectangular duct, secondary flow, unsteady solutions, Dean number and time evolution.

Nomenclature

Dn	: Dean number	T	: Temperature
Tr	: Taylor number	u	: Velocity components in the $x-$direction
Gr	: Grashof number	v	: Velocity components in the $y-$direction
h	: Half height of the cross section	w	: Velocity components in the $z-$direction
d	: Half width of the cross section	x	: Horizontal axis
L	: Radius of the curvature	y	: Vertical axis
P_r	: Prandtl number	z	: Axis in the direction of the main flow
t	: Time	λ	: Resistance coefficient

Greek letters

δ	: Curvature of the duct	μ	: Viscosity	υ	: Kinematic viscosity
ρ	: Density	κ	: Thermal diffusivity	ψ	: Sectional stream function

* Corresponding author. Tel.: +88-01710851580; Fax: +88-02-7113752.
E-mail address: rnmondal71@yahoo.com

1. Introduction

The study of flow and heat transfer in a curved ducts and channels has attracted considerable attention because of their ample applications in fluids engineering. Due to engineering applications and their intricacy, the flow in a rotating curved duct has become one of the most challenging research fields of fluid mechanics. Since rotating machines were introduced into engineering applications, such as rotating systems, gas turbines, electric generators, heat exchangers, cooling system and some separation processes, scientists have paid considerable attention to study rotating curved duct flows. The readers are referred to Nandakumar and Masliyah [1], Ito [2] and Yanase *et al.* [2] for some outstanding reviews on curved duct flows.

The fluid flowing in a rotating curved duct is subjected to two forces: the *Coriolis force* due to rotation and the *centrifugal force* due to curvature. For isothermal flows of a constant property fluid, the Coriolis force tends to produce vortices while centrifugal force is purely hydrostatic. When a temperature induced variation of fluid density occurs for non-isothermal flows, both Coriolis and centrifugal type buoyancy forces can contribute to the generation of vortices. These two effects of rotation either enhance or counteract each other in a non-linear manner depending on the direction of wall heat flux and the flow domain. Therefore, the effect of system rotation is more subtle and complicated and yields new; richer features of flow and heat transfer in general, bifurcation and stability in particular, for non-isothermal flows. Selmi *et al.* [4] examined the combined effects of system rotation and curvature on the bifurcation structure of two-dimensional flows in a rotating curved duct with square cross section. Wang and Cheng [5], employing finite volume method, examined the flow characteristics and heat transfer in curved square ducts for positive rotation and found reverse secondary flow for the co-rotation cases. Selmi and Nandakumer [6] and Yamamoto *et al.* [7] performed studies on the flow in a rotating curved rectangular duct. When a temperature induced variation of fluid density occurs for non-isothermal flows, both Coriolis and centrifugal type buoyancy forces can contribute to the generation of vorticity (Mondal *et. al.*, [8]). These two effects of rotation either enhance or counteract each other in a non-linear manner depending on the direction of wall heat flux and the flow domain. Therefore, the effect of system rotation is more subtle and complicated and yields new; richer features of flow and heat transfer in general, bifurcation and stability in particular, for non-isothermal flows. Very recently, Mondal *et al.* [9] performed numerical investigation of the non-isothermal flows through a rotating curved square duct and obtained substantial results. However, there is no known study on rotating curved rectangular duct flows with buoyancy effect. The present paper is, therefore, an attempt to fill up this gap. Studying the effects of rotation on the flow characteristics, caused by the buoyancy forces, is an important objective of the present study.

2. Mathematical Formulations

Consider a hydro-dynamically and thermally fully developed two-dimensional flow of viscous incompressible fluid through a rotating curved duct with rectangular cross section, whose height and wide are $2h$ and $2l$, respectively. The coordinate system with the relevant notation is shown in Fig. 1, where x' and y' axes are taken to be in the horizontal and vertical directions respectively, and z' is the axial direction. The system rotates at a constant angular velocity Ω_T around the y' axis. It is assumed that the outer wall of the duct is heated while the inner wall cooled. u, v and w be the velocity components in the x', y' and z' directions respectively. All the variables are non-dimensionalized.

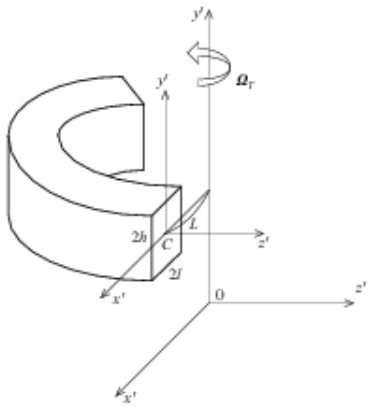

Figure 1: Coordinate system of the rotating curved duct

The sectional stream function ψ is introduced as

$$u = \frac{1}{1+\delta x}\frac{\partial \psi}{\partial \bar{y}}, \quad v = -\frac{1}{1+\delta x}\frac{\partial \psi}{\partial x} \tag{1}$$

Then, the basic equations for the axial velocity w, the stream function ψ and temperature T are expressed in terms of non-dimensional variables as:

$$(1+\delta x)\frac{\partial w}{\partial t} + \frac{\partial(w,\psi)}{\partial(x,y)} - Dn + \frac{\delta^2 w}{1+\delta x} = (1+\delta x)\Delta_2 w - \frac{\partial}{1+\delta x}\frac{\partial \psi}{\partial y}w + \delta\frac{\partial w}{\partial x} - \delta Tr\frac{\partial \psi}{\partial y}, \tag{2}$$

$$\left(\Delta_2 - \frac{\delta}{1+\delta x}\frac{\partial}{\partial x}\right)\frac{\partial \psi}{\partial t} = -\frac{1}{(1+\delta x)}\frac{\partial(\Delta_2\psi,\psi)}{\partial(x,y)}$$
$$+\frac{\delta}{(1+\delta x)^2}\left[\frac{\partial \psi}{\partial y}\left(2\Delta_2\psi - \frac{3\delta}{1+\delta x}\frac{\partial \psi}{\partial x} + \frac{\partial^2 \psi}{\partial x^2}\right) - \frac{\partial \psi}{\partial x}\frac{\partial^2 \psi}{\partial x \partial y}\right] + \frac{\delta}{(1+\delta x)^2} \tag{3}$$
$$\times\left[3\delta\frac{\partial^2 \psi}{\partial x^2} - \frac{3\delta^2}{1+\delta x}\frac{\partial \psi}{\partial x}\right] - \frac{2\delta}{1+\delta x}\frac{\partial}{\partial x}\Delta_2\psi + w\frac{\partial w}{\partial y} + \Delta_2{}^2\psi - G_r(1+\delta x)\frac{\partial T}{\partial x} + \frac{1}{2}Tr\frac{\partial w}{\partial y},$$

$$\frac{\partial T}{\partial t} + \frac{1}{(1+\delta x)}\frac{\partial(T,\psi)}{\partial(x,y)} = \frac{1}{\mathrm{Pr}}\left(\Delta_2 T + \frac{\delta}{1+\delta x}\frac{\partial T}{\partial x}\right) \tag{4}$$

The non-dimensional parameters Dn, the Dean number, Gr, the Grashof number, Tr, the Taylor number and Pr, the Prandtl number, which appear in equation (2) to (4) are defined as:

$$Dn = \frac{Gl^3}{\mu\upsilon}\sqrt{\frac{2l}{L}}, \; Gr = \frac{\beta g \Delta T\, l^3}{\upsilon^2}, \; Tr = \frac{2\sqrt{2\delta}\,\Omega_T l^3}{\upsilon\delta}, \mathrm{Pr} = \frac{\upsilon}{\kappa} \tag{5}$$

where the parameters denote their usual meaning. The rigid boundary conditions for w and ψ are used as

$$w(\pm1,y) = w(x,\pm1) = \psi(\pm1,y) = \psi(x,\pm1) = \frac{\partial \psi}{\partial x}(\pm1,y) = \frac{\partial \psi}{\partial y}(x,\pm1) = 0 \tag{6}$$

and the temperature T is assumed to be constant on the walls as:

$$T(1,y) = 1, \; T(-1,y) = -1, T(x,\pm1) = x \tag{7}$$

3. Numerical Methods

In order to solve the Equations (2) to (4) numerically, the spectral method is used. By this method the expansion functions $\phi_n(x)$ and $\psi_n(x)$ are expressed as

$$\left.\begin{aligned}\phi_n(x) &= (1-x^2)C_n(x),\\ \psi_n(x) &= (1-x^2)^2 C_n(x)\end{aligned}\right\} \tag{8}$$

Where $C_n(x) = \cos(n\cos^{-1}(x))$ is the n^{th} order Chebyshev polynomial. $w(x,y,t)$, $\psi(x,y,t)$ and $T(x,y,t)$ are expanded in terms of the expansion functions $\phi_n(x)$ and $\psi_n(x)$ as

$$\left.\begin{aligned} w(x,y,t) &= \sum_{m=0}^{M}\sum_{n=0}^{N} w_{mn}(t)\varphi_m(x)\varphi_n(y)\\ \psi(x,y,t) &= \sum_{m=0}^{M}\sum_{n=0}^{N} \psi_{mn}(t)\psi_m(x)\psi_n(y).\\ T(x,,y,t) &= \sum_{m=0}^{M}\sum_{n=0}^{N} T_{mn}\varphi_m(x)\varphi_n(y) + x \end{aligned}\right\} \tag{9}$$

where M and N are the truncation numbers in the x and y directions respectively. The accuracy of the numerical calculations is investigated for the truncation numbers M and N used in this study for the flow through a rotating curved rectangular duct. Five types of grid size (truncation number) were used to check the dependence of grid size (i.e. M and N).

For good accuracy of the solutions, N is chosen equal to $2M$. Variation of five representative properties with the grid size are taken as $14\times28,\ 16\times32, 18\times36, 20\times40, 22\times44$, and it is found that M = 20 and N = 40 give sufficient accuracy of the numerical solutions, which are not shown here for brevity. In order to calculate the unsteady solutions, the Crank-Nicolson and Adams-Bashforth methods together with the function expansion (9) and the collocation methods are applied to Eqs. (2) to (4).

4. Resistance coefficient

We use the resistance coefficient λ as one of the representative quantities of the flow state. It is also called the *hydraulic resistance coefficient*, and is generally used in fluids engineering, defined as

$$\frac{P_1^* - P_2^*}{\Delta z^*} = \frac{\lambda}{dh^*}\frac{1}{2}\rho\left\langle w^* \right\rangle^2, \tag{10}$$

where quantities with an asterisk denote the dimensional ones, $\langle\,\rangle$ stands for the mean over the cross section of the rectangular duct, and $d_h^* = 4(2l\times4lh)/(4l\times8lh)$. Since $\left(P_1^* - P_2^*\right)/\Delta z^* = G$, λ is related to the mean non-dimensional axial velocity $\langle w\rangle$ as

$$\lambda = \frac{16\sqrt{2\delta}Dn}{3\langle w\rangle^2}, \tag{11}$$

where $\langle w\rangle = \sqrt{2\delta}d/\nu\left\langle w^* \right\rangle$. In this paper, λ is used to calculate the unsteady solutions by numerical computations.

5. Results and Discussion

We take a curved rectangular duct and rotate it around the centre of curvature with an angular velocity Ω_T in both the positive and negative direction. Positive rotation means that the rotational direction is in the same direction as of the main flow while negative direction means that the rotational direction is opposite to the main flow direction. In this paper, time evolution calculations of the resistant coefficient λ are performed for the non-isothermal flows (Gr = 100) through a rotating curved rectangular duct over a wide range of the Dean Numbers (*Dn*) and the Taylor Number (*Tr*) for two cases of the duct rotation, *Case I*: Positive rotation and *Case II*: Negative rotation.

5.1 Case *I* : Positive Rotation

For positive rotation we perform time evolution of λ for $0 \le Tr \le 3000$ and $100 \le Dn \le 1000$. Figure 2(a) shows time evolution of λ for Tr = 1000 and Dn = 1000 at Gr = 100. It is found that the unsteady flow at Tr = 1000 and Dn = 1000 is a chaotic solution, which is well justified by drawing the phase spaces as shown in Fig. 2(b). Figure 2(c) shows typical contours of secondary flow patterns and temperature profiles for Tr = 1000 and Dn = 1000, where we find that the unsteady flow is a six- and eight-vortex solution. This is because as the Coriolis force and centrifugal force simultaneously increased the number of secondary vortices also increases (Wang and Cheng [10]). Then we perform time evolution of λ for Tr = 1300 and Dn = 1000 as shown in Fig. 3(a). It is found that the unsteady flow is a periodic solution at Tr = 1300 and Dn = 1000. In order to observe the periodic oscillation more clearly, we draw the phase space as shown in Fig. 3(b), and it is found that the flow is multi-periodic but not periodic. Typical contours of secondary flow patterns and temperature profiles are shown in Fig. 3(c) for one period of oscillation, and we see that the multi-periodic solution at Tr = 1300 and Dn = 1000 is a five-vortex solution. Then we perform time evolution of λ for Tr = 1000 and Dn = 1500 at Gr = 100 as shown in Fig. 4(a). It is found that the unsteady flow at Tr = 1000 and Dn = 1500 is also a multi-periodic solution, which is justified by drawing the phase space as shown in Fig. 4(b). Typical contours of secondary flow patterns and temperature profiles are shown in Fig. 4(c), and it is found that the multi-periodic solution at Tr = 1300 and Dn = 1500 is a two-vortex solution. If we increase the rotational speed more, for example Tr = 2000, we see that the flow becomes steady-state as shown in Fig. 4(d).

(a)

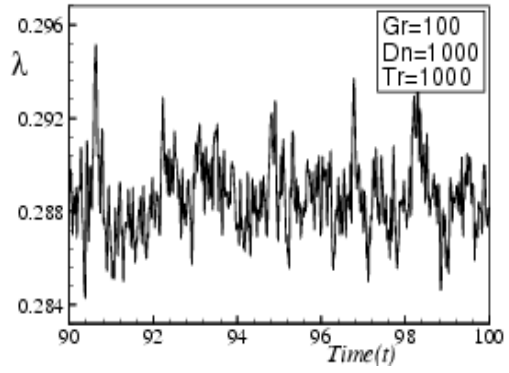

(b)

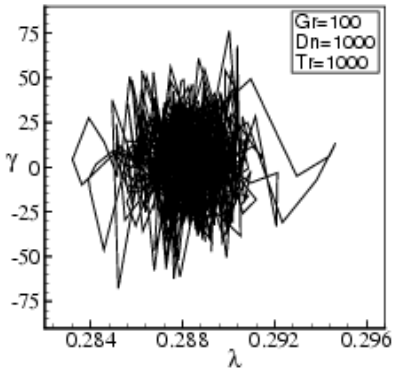

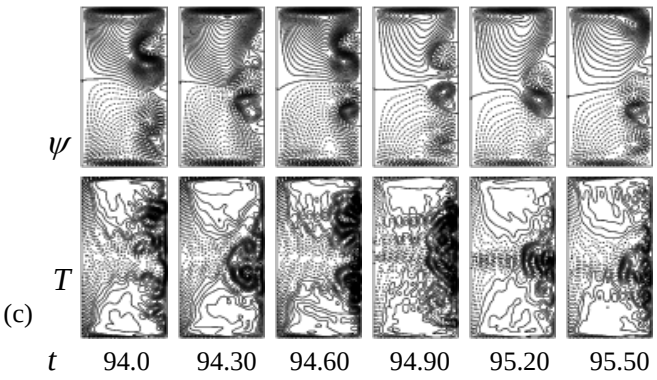

Figure 2: (a) Time evolution of λ for Tr = 1000 and Dn = 1000 at Gr = 100, (b) Phase space for Tr = 1000 and Dn = 1000, (c) Contours of secondary flow patterns (top) and temperature profiles (bottom) for Tr = 1000 and Dn = 1000 at time $94.0 \le t \le 95.5$.

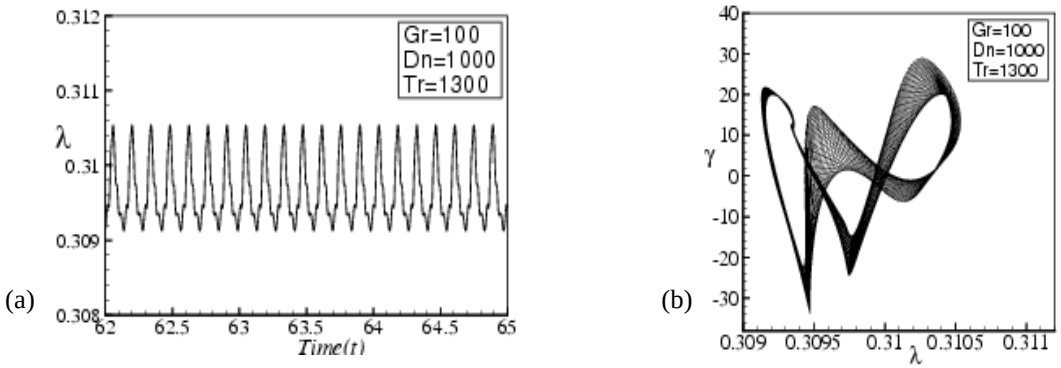

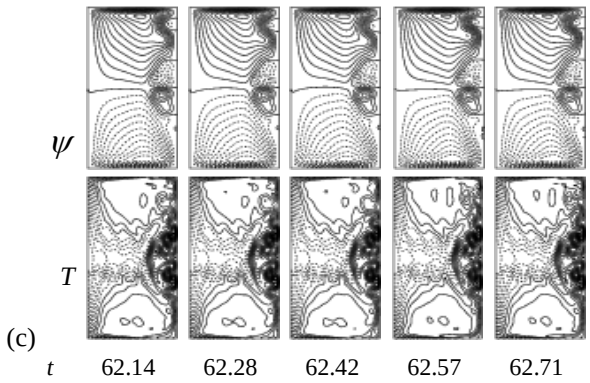

Figure 3: Time evolution of λ for Tr = 1300 and Dn = 1000 at Gr = 100, (b) Phase space for Tr = 1300 and Dn = 1000, (c) Contours of secondary flow patterns (top) and temperature profiles (bottom) for Tr = 1300 and Dn = 1000 at time $62.14 \le t \le 62.71$.

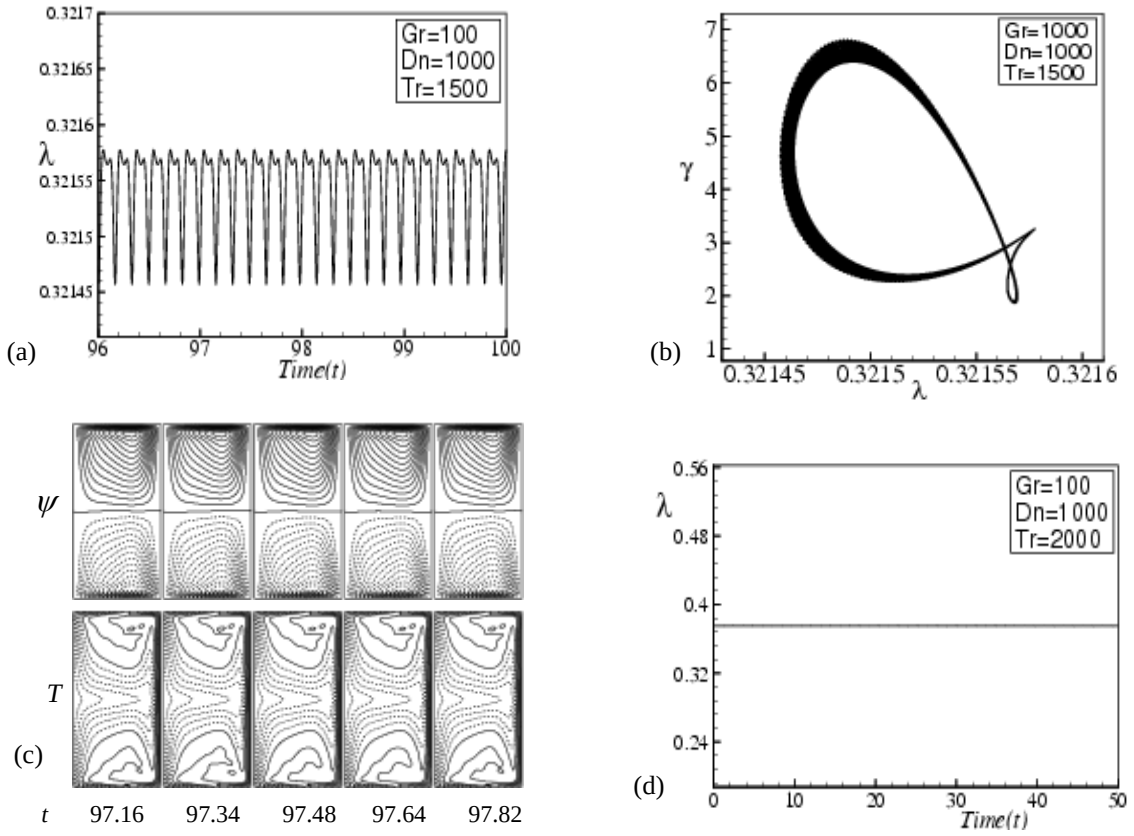

Figure 4: Time evolution of λ for Tr = 1500 and Dn = 1000 at Gr = 100, (b) Phase space for Tr = 1500 and Dn = 1000, (c) Contours of secondary flow patterns (top) and temperature profiles (bottom) for Tr = 1500 and Dn = 1000 at time $97.16 \le t \le 97.82$, (d) Time evolution of λ for Tr = 2000 and Dn = 1000 at Gr = 100.

5.2 Case *II*: Negative Rotation

For the negative rotation, we rotate the duct in opposite direction of the main flow direction and the flow structure becomes more complicated. We perform time evolution of λ for the negative rotation $-1000 \le Tr \le -100$ over the Dean number $100 \le Dn \le 1000$. Figure 5(a) shows time evolution of λ for Tr = -100 and Dn = 700 at Gr = 100, and it is found that the unsteady flow is a chaotic solution for Tr = -100 and Dn = 700. The chaotic oscillation is well justified by drawing the phase spaces as shown in Fig. 5(b). Figure 5(c) shows typical contours of secondary flow patterns and temperature profiles for Tr = -100 and Dn = 700, where we find that the unsteady flow is a two- and four-vortex solution. Then we perform time evolution of λ for Tr = -200 and Dn = 700 as shown in Fig. 6(a). It is found that the unsteady flow is a periodic solution at Tr = -200 and Dn = 700. In order to observe the periodic oscillation more clearly, we draw the phase space of the time evolution result as shown in Fig. 6(b), and it is found that the unsteady flow at Tr = -200 and Dn = 700 is purely a periodic solution. To observe the pattern variation of secondary flows and heat transfer, as time proceeds, typical contours of secondary flow patterns and temperature profiles are shown in Fig. 6(c) for Tr = -200 and Dn = 700, and we find that the periodic solution at Tr = -200 and Dn = 700 is a two-vortex solution. If we increase rotational speed in the negative direction more, for example Tr = -300, we see that the flow becomes steady-state as shown in Fig. 6(d) for Tr = -300 and Dn = 700. If we increase the rotational speed in the negative direction up to Tr = -1000, we find that the flow remains steady-state. All the time evolution results are not shown here for brevity. It is found that as the coriolis force is increased in the negative direction keeping the centrifugal force fixed at moderate Dn numbers, the flow ceases to be steady state; this is because the Coriolis force and centrifugal force counteract each other at low Dean numbers, which results in formation of few secondary vortices at the outer wall of the duct.

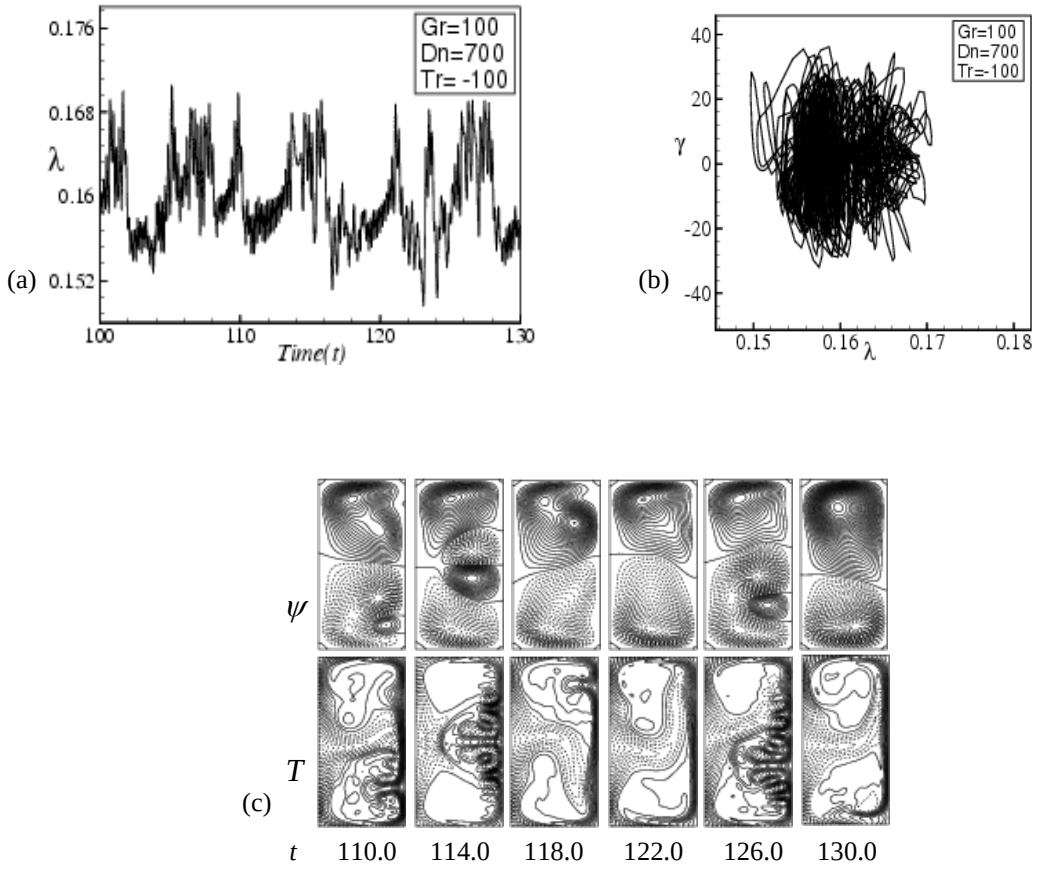

Figure 5: Time evolution of λ for Tr = -100 and Dn = 700 at Gr = 100, (b) Phase space for Tr = -100 and Dn = 700, (c) Contours of secondary flow patterns (top) and temperature profiles (bottom) for Tr = -100 and Dn = 700 at time $110 \le t \le 130$.

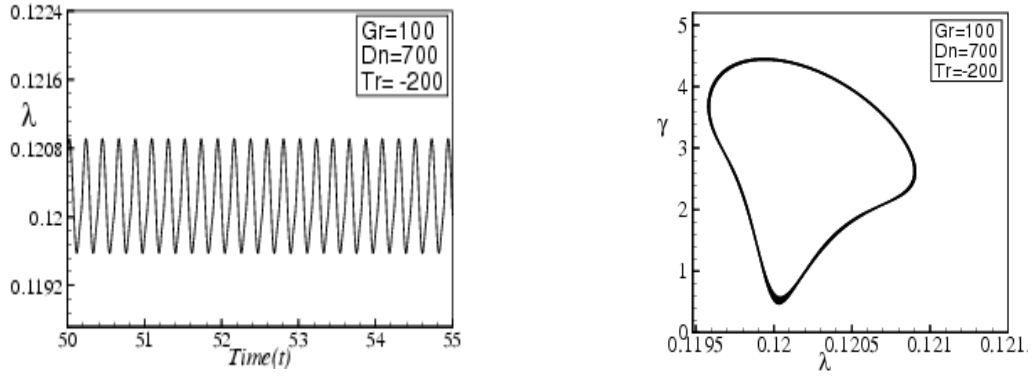

(a) (b)

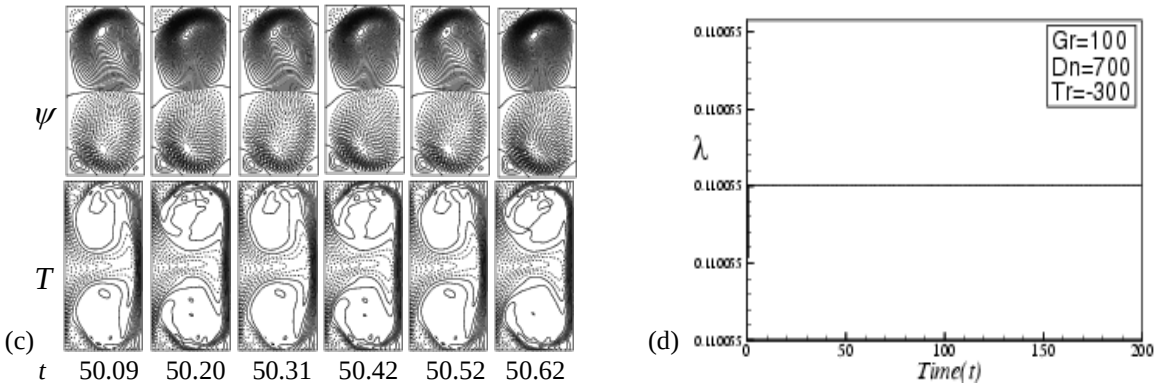

Figure 6: Time evolution of λ for Tr = -200 and Dn = 700 at Gr = 100, (b) Phase space for Tr = -200 and Dn = 700, (c) Contours of secondary flow patterns (top) and temperature profiles (bottom) for Tr = -200 and Dn = 700 at time $50.09 \le t \le 50.62$, (d) Time evolution of λ for Tr = -300 and Dn = 700 at Gr = 100.

6. Conclusion

A numerical study is presented for the flow characteristics through a rotating curved rectangular duct of constant curvature $\delta = 0.1$. Numerical calculations are carried out by using a spectral method, and covering a wide range of the Taylor number $-1000 \le Tr \le 3000$ and the Dean number $100 \le Dn \le 1000$ for the Grashof number $Gr = 100$. For positive rotation, we investigate the unsteady flow characteristics for the Taylor number $0 \le Tr \le 3000$ and it is found that the unsteady flow undergoes in the scenario '*Chaotic* $\rightarrow$ *multi-periodic* $\rightarrow$ *periodic* $\rightarrow$ *steady-state'*, if *Tr* is increased in the positive direction. For negative rotation, however, we investigate the unsteady flow behavior for $-1000 \le Tr \le -100$, and it is found that the unsteady flow undergoes through '*Chaotic* $\rightarrow$ *multi-periodic* $\rightarrow$ *periodic* $\rightarrow$ *steady-state*', if *Tr* is increased in the negative direction. Typical contours of secondary flow patterns and temperature profiles are also obtained at several values of *Tr*, and it is found that there exist two-, four-, six- and eight-vortex solutions if the duct rotation involved in both positive and negative direction. It is found that the temperature distribution is consistent with the secondary vortices, and convective heat transfer is enhanced as the secondary vortices increase. It is also found that chaotic flow enhances heat transfer significantly than the periodic or steady-state solutions.

References

[1] Nandakumar, K. and Masliyah, J. H. (1986). Swirling Flow and Heat Transfer in Coiled and Twisted Pipes, *Adv. Transport Process*., Vol. **4**, pp. 49-112.

[2] Ito, H (1987). Flow in curved pipes. *JSME International Journal*, **30**, 543–552.

[3] Yanase, S., Kaga, Y. and Daikai, R. (2002). Laminar flow through a curved rectangular duct over a wide range of the aspect ratio, *Fluid Dynamics Research*, Vol. **31,** pp. 151-183.

[4] Selmi, M. and Namdakumar, K. and Finlay W. H., 1994. A bifurcation study of viscous flow through a rotating curved duct, *J. Fluid Mech.* Vol. **262**, pp. 353-375.

[5] Wang, L. Q. and Cheng, K.C., 1996. Flow Transitions and combined Free and Forced Convective Heat Transfer in Rotating Curved Channels: the Case of Positive Rotation *Physics of Fluids*, Vol. **8**, pp.1553-1573.

[6] Selmi, M. and Namdakumar, K. (1999). Bifurcation Study of the Flow through Rotating Curved Ducts, *Physics of Fluids*, Vol. **11**, pp. 2030-2043.

[7] Yamamoto, K., Yanase, S. and Alam, M. M. (1999). Flow through a Rotating Curved Duct with Square Cross-section, *J. Phys. Soc*. Japan, Vol. **68**, pp. 1173-1184.

[8] Mondal, R. N., Alam M. M. and Yanase, S. (2007). Numerical prediction of non- isothermal flows through a rotating curved duct with square cross section, *Thommasat Int. J. Sci and Tech.*, Vol. **12**, No. 3, pp. 24-43.

[9] Mondal, R. N., Datta, A. K. and Uddin, M. K. (2012). A Bifurcation Study of Laminar Thermal Flow through a Rotating Curved Duct with Square Cross-section, *Int. J. Appl. Mech. and Engg.* Vol. **17** (2). (In Press).

[10] Wang, L. Q. and Cheng, K.C. (1996). Flow Transitions and combined Free and Forced Convective Heat Transfer in Rotating Curved Channels: the Case of Positive Rotation, *Physics of Fluids*, Vol. **8**, pp.1553-1573.

Available online at www.sciencedirect.com

SciVerse ScienceDirect

Procedia Engineering 00 (2012) 000–000

Procedia Engineering

www.elsevier.com/locate/procedia

5th BSME International Conference on Thermal Engineering

Numerical simulation of supersonic mixing layers for parallel and non-parallel streams

Mohammad Ali*, M Quamrul Islam, TAGMZN Jubery, Sanchita Amin

Bangladesh University of Eengineering & Technology, Dhaka-1000, Bangladesh

Abstract

In this study supersonic mixing of two-parallel and non parallel gaseous streams has been simulated numerically. The streams are of air and hydrogen, which come into contact after passing over a finite thickness base. Two gas streams are considered from a high-pressure reservoir and entering into the domain with atmospheric pressure. Two-dimensional unsteady state Navier-Stokes equations, energy, mass diffusion and species continuity equations are numerically simulated to analyze the two-dimensional mixing layer in supersonic flow field. An explicit Harten-Yee Non-MUSCL Modified flux-type TVD (total variation diminishing) scheme has been used to solve the system of equations. An algebraic turbulence model is used to calculate the eddy viscosity coefficient. Keeping constant the inlet pressure and velocity of the streams, the merging angle is varied to observe the physics of flow fields, mixing fields of two-streams and mixing efficiency. The result shows that when merging angle increases interaction between two streams, high momentum exchange occurs and eventually enhances the mixing of two streams.

Keywords: Supersonic combustor, mixing, shear layers, merging angle

1. Introduction

Turbulent mixing layers occur in flow fields of many engineering applications e.g., combustion chambers, pre-mixers for gas turbine combustors, chemical lasers, propulsion systems and flow reactors. Particularly, the mixing of reactants and their complete combustion in supersonic combustion ramjet (scramjet) engines has drawn special attention of present scientists. In supersonic combustion systems, the flow speeds are so high that the fuel and oxidizer have little time to mix. The shear layers are naturally unstable and usually lead to a large scale mixing. The higher the Mach number, the longer length it takes for the shear layers to become unstable. This reduces mixing accomplished in a given length. Several configurations of combustor have been studied to seek the enhancement of mixing. Generally parallel, normal or oblique type mixing is used and most of the researchers carried out their study on two parallel supersonic streams.

Guirguis et al. [1] performed two-dimensional time-dependent numerical simulation of the convective mixing of two supersonic parallel streams of air. They simulated a supersonic shear layer in a two dimensional channel of 20 cm long and 2.4 cm high and used flux corrected transport algorithm neglecting all diffusion transport processes. Comparisons were made for the vorticity, density and pressure contour of confined and unconfined shear layer. Farouk et al. [2] performed numerical simulation of the mixing of two supersonic streams of air in a 25cm x 3cm flow field considering laminar velocity profile of the streams at inlet. They solved Euler equation and studied the effects of density, velocity and pressure variation on mixing. Brown et al. [3] experimentally investigated the effects of density ratio on plane turbulent mixing between two streams of different gases. It was observed that, for all ratios of densities in the two streams, the mixing layer was dominated by large coherent structures. These structures made convection at nearly constant speed, and increased their sizes and spaces

* Corresponding author. Tel.: +88-01732194776; fax: +88-02-8613046.
E-mail address: mali@me.buet.ac.bd

discontinuously by the process of amalgamation with neighboring ones. Papamoschuo et al. [4] observed that the spreading rate was dependent on Mach number but independent on transverse density gradients.

Ali and Islam [5] studied the mixing mechanisms, investigated the mixing characteristics for several flow configurations and observed that recirculation in flow field can play an important role in the mixing enhancement. Ali et al. [6] found that the inlet configuration of air stream can play an important role on the enhancement of mixing. Ali et al. [7] studied the physics of mixing in two-dimensional supersonic stream and showed that mixing is only possible by incorporating the molecular diffusion terms in the Navier-Stokes equations. Gerlinger et al. [8] found that increase in injector lip thickness results in increased shear layer thickness and also in larger total pressure losses because of the stronger recompression shocks. They also found that increase in mixing layer thickness did not have significant effect on the mixing efficiency. In another investigation Guirguis et al. [9] studied the effect of bluff center bodies on mixing enhancement in supersonic shear layers. They observed that the shear layer became unstable faster than with the streamlined body. As a result, a large amount of convective mixing occurs within the length of the domain. Azim et al. [10] investigated plane mixing layers from parallel and non-parallel merging of two streams. The authors reported that both types of mixing layers were found to decrease in growth with increasing velocity ratio, though they spread more at the high speed side.

In present research, numerical investigation on supersonic mixing layers has been performed by solving two-dimensional unsteady Navier-Stokes equations, energy equation, mass diffusion equation and continuity equation. The problem was defined by allowing two streams past over a finite-thickness base (2.3 mm) confined between two parallel plates. The air stream is at the upper side of the base plate and the hydrogen stream is underneath the base plate as shown in Fig. 1. After separating from the base, the streams form shear layers and mix with one another that usually occurs in combustor. This study has been made for the following reasons: (i) to increase the mixing efficiencies of a supersonic combustor and (ii) to study the physics of fluid dynamics including shocks and turbulence. The inlet pressure ratio and velocity ratio of the two streams have been kept constant which is equal to unity and the merging angle is varied from 0 ~ 20º with the increment of 5º for this study. The calculations of flow field with different merging angles are denoted as case 1 (merging angle 0º), case 2 (merging angle 5º), case 3 (merging angle 10º), case 4 (merging angle 15º), and case 5 (merging angle 20º).

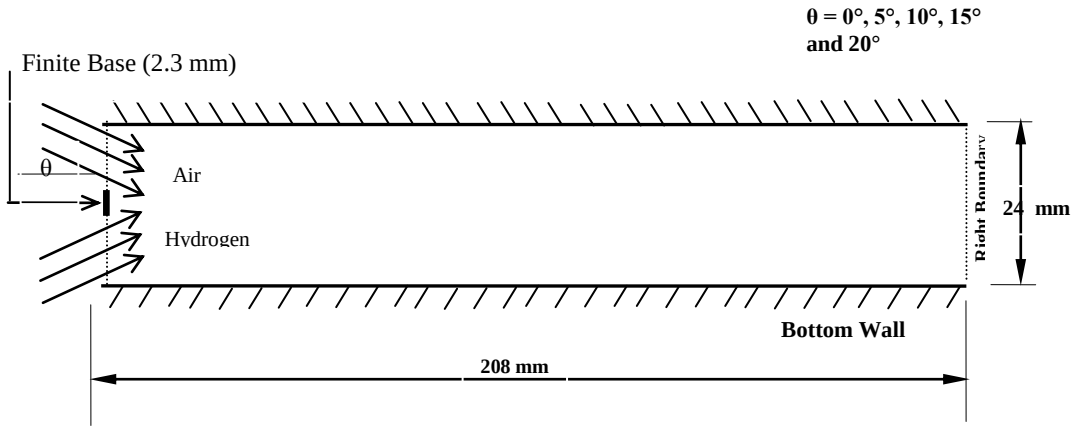

Fig. 1. Scematic diagram of the calculation domain

2. Governing equations and boundary conditions

The following continuity equation, Navier-Stokes equation, energy equation and mass diffusion equation are used to solve this flow field where body forces are neglected.

Continuity equation: $$\frac{\partial}{\partial t}(\rho)+\frac{\partial}{\partial x}(\rho u)+\frac{\partial}{\partial y}(\rho v)=0$$

Navier-Stokes equation: X component: $$\frac{\partial}{\partial t}(\rho u)+\frac{\partial}{\partial x}(p+\rho u^2)+\frac{\partial}{\partial y}(\rho uv)=\frac{\partial}{\partial x}(\sigma_x)+\frac{\partial}{\partial y}(\tau_{xy})$$

Y Component: $$\frac{\partial}{\partial t}(\rho v)+\frac{\partial}{\partial x}(\rho uv)+\frac{\partial}{\partial y}(p+\rho v^2)=\frac{\partial}{\partial x}(\tau_{yx})+\frac{\partial}{\partial y}(\sigma_y)$$

Energy equation: $$\frac{\partial}{\partial t}(E)+\frac{\partial}{\partial x}[(E+p)u]+\frac{\partial}{\partial y}[(E+p)v]=\frac{\partial}{\partial x}[u\sigma_x-v\tau_{xy}-\dot{q}_x]+\frac{\partial}{\partial y}[u\tau_{yx}-v\sigma_y-\dot{q}_y)]$$

Species continuity equation: $$\frac{\partial}{\partial t}(\rho Y_i)+\frac{\partial}{\partial x}(\rho Y_i u)+\frac{\partial}{\partial y}(\rho Y_i v)+\frac{\partial}{\partial x}(\dot{m}_{ix})+\frac{\partial}{\partial y}(\dot{m}_{iy})=0$$

- The top and bottom boundaries of the computational region are considered as solid walls. A Navier-Stokes analysis imposes that the normal and tangential velocity components are zero on the walls. The walls are assumed to be thermally adiabatic, so that $(\partial T/\partial n)_w = 0$.
- Inflow boundary conditions are used on the left boundary of the computational domain. The inflow condition is supersonic with fully developed turbulent boundary layers which is kept constant throughout the computations.
- The outflow boundary conditions (X = L) are considered to be zero-gradient for all variables.

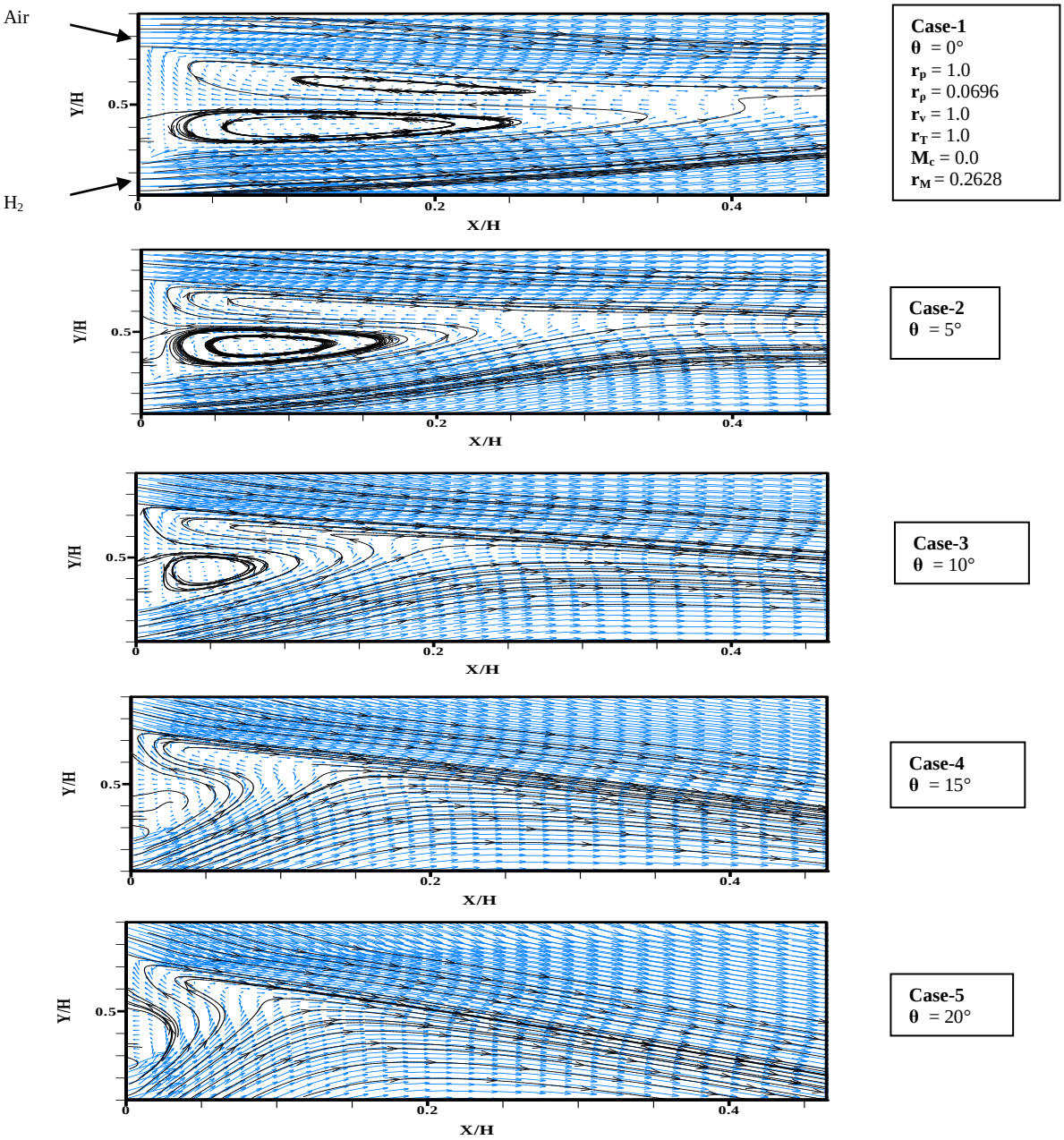

Fig 2. Vector and streamline representation of near flow circulating region for all cases.

3. Results and discussion

3.1 Physics of fluid dynamics

Figure 2 shows the velocity vectors with streamlines just behind the finite base for case 1~5. In Fig 2(a) the upper recirculation rotates clockwise while the lower recirculation rotates counterclockwise. The flows expand and high interaction occurs after recirculation. The recirculation zones spread downstream, increasing the length in longitudinal direction. The stream lines indicate that both of the recirculations are created by the hydrogen flow. For other cases in Figs. 2(b) to (e), after entering into the first recirculation, portion of the hydrogen flow cannot complete the recirculation. This portion of hydrogen makes intimate contact with air and deflects 180° due to the high momentum of air stream. The velocity in recirculation is low and therefore hydrogen has much time to contact with air resulting in high diffusion. Throughout the study, the momentum of air is higher than that of hydrogen, due to which the expansion of hydrogen is high behind the base while the expansion of the air stream is low. Due to expansion and interaction between two streams hydrogen enters in the recirculation region and mixes with air by diffusion and convection. So recirculation plays a vital role to enhance mixing.

Figure 2(b) shows the shear layer mixing regions spread with longitudinal distance until impingement occurs at approximately X/H = 0.225, which is shorter than case 1. Therefore, the area of recirculation zones in case-2 are smaller than case-1. Figures 2(a~e) shows that with the increment of merging angle the size of both recirculations diminishes but more hydrogen molecules are entering in the recirculation region due to strong interactions and eventually more molecular and convection diffusion occurs. Another observation is that in Fig. 2(a) two recirculations are very clear but in Fig. 2(b) the upper recirculation vanishes and the size of lower recirculation decreases. Moreover, the streamlines generated from the same location of Fig. 2(a~b) indicate that more hydrogen molecules enter into the upper side of the recirculation region and make intimate contact with the air stream for case 2 than that of case 1. Velocity distribution curve in Fig. 3 shows that velocities of the upper section are similar for all merging angles at constant pressure ratio. But the velocity of the lower part (hydrogen) increases at the downstream. The maximum velocity occurs at very low merging angles of 20. The maximum velocity 3200 m/s is found at X/H= 5.98 for pressure ratio 1.0.

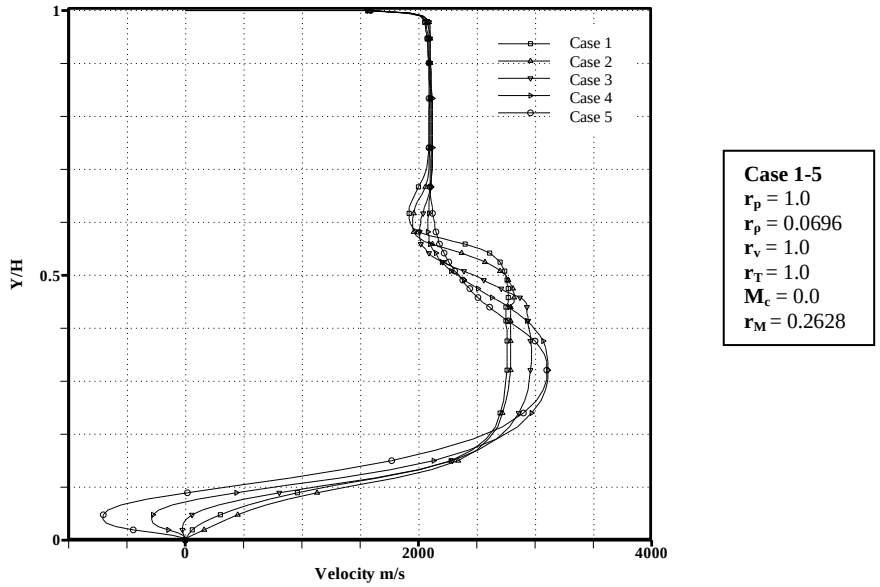

Fig. 3. Velocity distribution at section X/H=5.98 for Case 1 to Case 5

3.2 Structure of shear layers

The mole fraction contours give a structure of free shear layers created by the mixing of the two streams. Figure 4 shows the mole fraction contours of hydrogen for pressure ratio 1.0. The mole fraction of hydrogen close to bottom wall is 0.95 and the contour line varies from 0.95 to 0.05 towards the upper wall. The increment of mole fraction between two adjacent contour lines is 0.05. As stated earlier, a thin base is located from Y/H = 0.45 to 0.55 in the middle of the two streams. Throughout the study hydrogen has less momentum than that of the air stream and eventually hydrogen will occupy more space after the thin base. For case 1, there is no initial deflection of shear layer due to identical pressure. But for cases 2-5, the shear layer deflects towards the bottom wall due to non-parallel mixing and higher density of air. The deflection angles

for case 2, 3, 4 and 5 are 5.0º, 8.0º, 10.0º and 18.0º, respectively. The spreading rate of free shear layers increases with the increment of merging angle. Further deflections of shear layer at downstream are fairly understandable for higher merging angles.

3.3 Mixing efficiency

Mixing efficiency has been calculated on the basis of flammability limits of hydrogen and air. So, in the calculation of mixing efficiency the region having the mole fraction range of hydrogen from 0.05 to 0.75 has been taken into consideration. The mixing of hydrogen in air can be occurred by means of (i) interaction between two streams, (ii) turbulence and convection due to recirculation and velocity of the flow, or (iii) molecular diffusion due to density gradient. The performance of different cases is evaluated by calculating the mixing efficiency. Figure 5 shows the mixing efficiency along the physical model for different cases. For all the cases the mixing efficiency increases sharply just behind the base due to expansion at the thin base corner and recirculation. The rate of increment in efficiency further increases due to the interaction of two streams. In downstream the mixing is very slow in mixing shear-layer because weak molecular diffusion due to supersonic nature of the flow.

Figure 5 shows the mixing efficiency along the physical model for cases 1~5. Generally, in the upstream region, the increasing of mixing is high and in downstream it is very slow. In Fig.6 at X/H= 2 the mixing efficiencies of the cases 1, 2, 3, 4 and 5 are approximately 5.0, 6.0, 8.5, 14.0 and 20.5%, respectively, i.e., in upstream mixing efficiency increases with the increase of mixing angle. Also increment of mixing can be found along the length of physical model between X/H = 4.0 to 5.0 for all the cases due to the impingement of the streams. In downstream, cases 3, 4 and 5 have negligible increment of mixing in the shear layer. Case 1 has the maximum increment of mixing at downstream. The difference between the value of mixing efficiency of cases 1 and 2 starts to decrease from X/H = 4.0 and the efficiency curve of case 1 coincides with that of case 2 at X/H = 7.0 and both curves coincide the curve of case 3

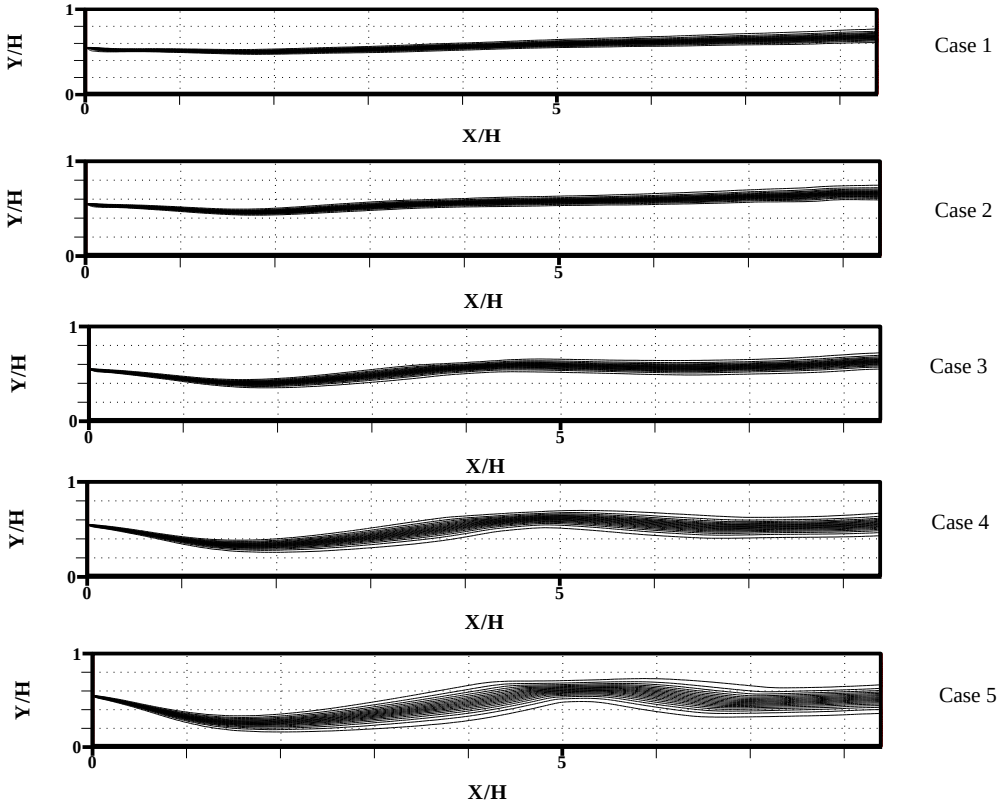

Fig. 4. Mole fraction contour of hydrogen φ(0.05,0.95,0.05) for different cases**.**

4. Conclusions

For good combustion in a supersonic combustor the efficient mixing is mandatory. Many experiments, theoretical and numerical studies have been performed on mixing, ignition and combustion in supersonic flow. In supersonic combustion,

high penetration and mixing of fuel with oxidizer is difficult due to their short residence time in combustor. In the present study the effects of merging angle (ranges from 0 ~ 20º) on supersonic mixing have been studied. Due to finite base, hydrogen and air expand behind the base creating a separation region and a recirculation region. Both hydrogen and air streams move to each other and strike behind base. The velocity in recirculation is low and therefore hydrogen has much time to contact with air resulting in high diffusion. By varying merging angle it has been found that, interaction between the two streams increases with increase of merging angle but the area of recirculation decreases. By the detail investigation of the recirculation region, it has been found that although recirculation area decreases with the increase of merging angle, high amount of hydrogen enters into the recirculation region and eventually mixing efficiency increases. Due to high interaction of the streams high momentum exchange occurs and eventually high mixing occurs at upstream for high merging angle. At high merging angle shocks created in the flow-field are strong. Due to these strong shocks, pressure loss increases as the merging angle increases. Strong interactions and shocks in high merging angles reduce the pressure in outflow boundary.

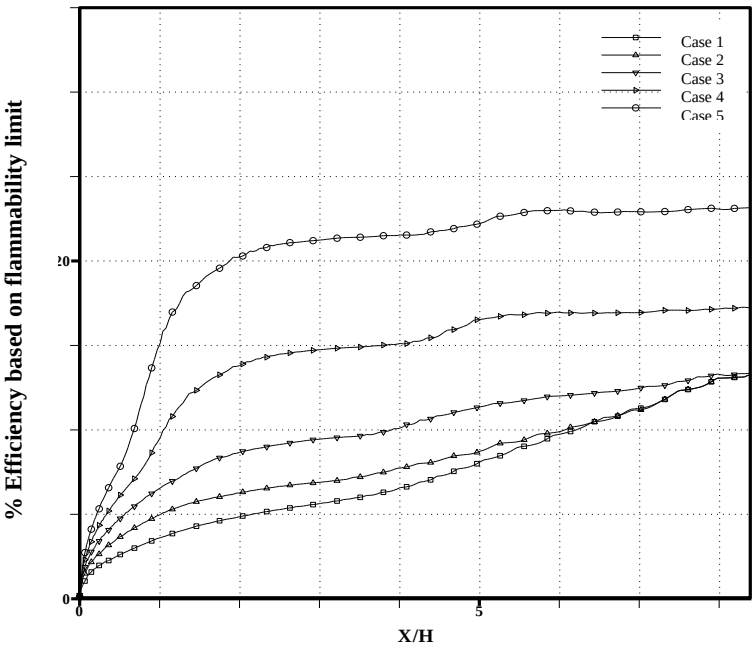

Fig. 5. Mixing efficiency based on flammability limit for different cases.

Acknowledgements

The authors are grateful to Bangladesh University of Engineering and Technology (BUET), Dhaka, Bangladesh to provide computation facilities and other financial support for this research.

5. References

[1] Guirguis, R.H., Girnstein, F. F. Young, T. R. Oran, E. S. Kailashanath, K. and Boris, J. P., 1987, "Mixing Enhancement in Supersonic Shear Layers", AIAA 87-0373.

[2] Farouk, B., Oran, E. S. and Kailashanath, K., 1991, "Numerical Simulations of the structure of supersonic shear layers", Physics of Fluids, A, Vol. 3, No. 11, p. 2786-2798.

[3] Brown, G.L., Roshko, A., 1974, "On Density Effects and Large Structure in Turbulent Mixing Layers", Journal of Fluid Mechanics, Vol. 64, No. 4, p. 775-816.

[4] Papamoschuo D., Roshko, A., 1988, "The Compressible Turbulent Shear Layer: An Experimental Study", Journal of Fluid Mechanics, 197, p. 453-477.

[5] Ali, M. and Islam, A.K.M.S., 1999, "Effect of Main flow Inlet Width on Penetration and Mixing of Hydrogen in Scramjet Combustor", Proceedings of the Eighth Asian Congress of Fluid Mechanics, p. 647-650, December 6-10, Shenzhen, China.

[6] Ali, M., Fujiwara, T. and Leblanc, J.E., 2000, "Influence of Main Flow inlet Configuration on Mixing and Flame Holding in Transverse Injection into Supersonic Air Stream", International Journal of Engineering Science, 38, p.1161-

1180.
[7] Ali, M., Fujiwara, T. and Parvez, A., 2002, "A Numerical Study on the Physics of Mixing in Two-dimensional Supersonic Stream", Indian Journal of Engineering and Materials Sciences, 9, p.115-127.
[8] Gerlinger, P. and Bruggemann, D., 2000, "Numerical Investigation of Hydrogen Injections into Supersonic Airflows", Journal of Propulsion & Power, 16, p.22-28.
[9] Guirguis, R.H. Girnstein, F. F. Young, T. R. Oran, E. S. Kailashanath, K. and Boris, J. P., "Mixing Enhancement in Supersonic Shear Layers: II. Effect of Bluff Centre Bodies", Laboratory for Computational Physics and Fluid Dynamics, Naval Research Laboratory, Washington, D.C., Report- 20375
[10] Azim, M. A. and Islam, A.K.M.S., 2003, "Plane Mixing Layers from Parallel and Non-parallel Merging of Two Streams", Experiments in Fluids, 34, p. 220-226.

Available online at www.sciencedirect.com

SciVerse ScienceDirect

Procedia Engineering 00 (2012) 000–000

Procedia Engineering

www.elsevier.com/locate/procedia

5th BSME International Conference on Thermal Engineering

Application of Chevron Nozzle to a Supersonic Ejector–Diffuser System

Fan Shi Kong[a], Heuy Dong Kim[a*], Yingzi Jin[b] and Toshiaki Setoguchi[c]

[a]*Zhejiang Sci-Tech Univercity, China (Currently, School of Mechanical Engineering, Andong National University, Andong, Korea)*
[b]*College of Mechanical Engineering & Automation, Zhejiang Sci-Tech University, Hangzhou, China*
[c]*Department of Mechanical Engineering, Saga University, Japan*
**Corresponding author Email: kimhd@andong.ac.kr*

Abstract

The supersonic ejector-diffuser system was widely used in many industrial applications. Recently, it is also being used as one of the most important components of the solar seawater desalination facility. That is because this system has many advantages over other fluid machinery like no moving parts and no direct mechanical energy input. The system makes use of high-speed primary stream to entrain the secondary stream through pure shear action for the purposes of transport or compression of fluid. However, the optimization of the ejector-diffuser system and its optimal operation condition are hardly known due to the complicated turbulent mixing, compressibility effects and even flow unsteadiness which are generated inside the ejector-diffuser system. Much effort has devoted to the performance improvement of the system since it bears relatively very low efficiency. The optimization of the ejector-diffuser system and its performance improvement are of practical importance in industrial field. In the present study, a Chevron nozzle was applied to activate the shear actions between the primary and secondary streams, by means of longitudinal vortices generated from the Chevron. A CFD method has been applied to simulate the ejector-diffuser flow field. The present CFD results were validated with existing experimental data. The operation characteristics of the ejector system were compared between Chevron nozzle and conventional convergent nozzle for the primary stream. The ejector-diffuser system performance is discussed in terms of the entrainment ratio, ejector efficiency, pressure recovery as well as total pressure loss.

Keywords: Ejector-Diffuser System, Chevron Nozzle, Shock Wave, Compressible Flow, Supersonic Flow

Nomenclature

A	Cross-sectional area of supersonic nozzle exit (m^2)
D	Diameter of particular position (mm)
L	Length of particular position (mm)
M	Mach number at primary stream nozzle exit
P	Pressure (Pa)
P_d	Dynamic pressure (Pa)
P_s	Static pressure of particular position (or static pressure at nozzle exit if no subscript) (Pa)
P_t	total pressure (Pa)
P	Pressure recovery
R	Gas constant (J/kg•K)
Rm	Entrainment ratio: Ratio of two mass flow rates of primary and secondary stream using convergent nozzle
T	Temperature (K)
T_s	Static temperature (K)
T_t	Total temperature (K)
V	Velocity of primary stream (m/s)
x	Cartesian axis direction
y	Cartesian axis direction
y+	Non-dimensional distance

Greek letters

γ	Ratio of specific heats
ṁ	Mass flow rate of particular position (or mass flow rate at nozzle exit if no subscript)(kg/s)
ρ	Density

Subscripts

1	1st: Values at supersonic nozzle exit
2	2nd: Values at secondary stream inlet
e, E	Exit: Supersonic ejector-diffuser system exit
M	Mixing chamber of ejector-diffuser system
D	Diffuser section of ejector-diffuser system

1. Introduction

A supersonic ejector-diffuser system makes use of high pressure primary stream to propel the secondary stream through pure shear action for the purposes of transport or compression of fluid. Indeed, it can be used in many complex progresses as a compressor, a fluid transport component or a vacuum pump [1, 2, 3]. Along the development of solar industry, the ejector application in solar refrigeration and solar desalination was growing rapidly. At the same time, the ejector-diffuser system was increasingly considered as the most important equipment in these energy industries [4].

In the ejector itself, the primary stream with high pressure and high speed flowed out from the supersonic nozzle exit. Secondary stream was entrained by the primary stream and mixed up in the mixing chamber. At the end of the mixing chamber, two streams were completely mixed and the pressure was assumed to be constant until they reached the diffuser section [5, 6]. Complicated turbulent mixing, compressibility effects and even flow unsteadiness are like big obstacles restrict the studies on the ejector. Many researching works have been done to increase the performance of the ejector, but results were still unsatisfactory, compared with other industrial machineries [4]. Considering the complexity and difficulty on the researching, how to enhance the performance of ejector effectively became a significant task.

In the past decades, many researchers have done many significant works based on ejector geometry, nozzle design, and fluid selection. Aphornratana and Eames [7] performed an experiment to study refrigerator using a small scale steam ejector and a supersonic nozzle. Similar experiments have also been performed by [1, 6] based on nozzle design. Ouzzane and Aidoun [8] invented a new mathematical model of the ejector-diffuser; and the detailed structure was analyzed using 1-Dimensional compressible flow analysis. At the same time, a series of experimental works have been carried out to study the effect of ejector performance, especially in the effect of working fluids. In the present works, the modeling technique based on numerical software has been widely used to investigate the flow factors inside the ejector. Bartosiewicz et al. [9] compared static pressure distribution between experimental results and numerical simulation in different turbulence models. Many recent studies [9, 10] showed that computational results were expected to provide a reasonable cost and a visual display of local flow filed.

Researchers got a lot of good results based on geometrical optimization, but the study of internal structure has got little attention [11]. In the Texas A&M University, a researching team put forward an optimal method with a mixing guide vane installed at the inlet of ejector [12]. A productive experimental work of this ejector has been made by Manohar [13], and Somsak W. [14, 15] has finished the basic computational analysis in his doctoral dissertation. The geometrical model they were used was widely applied in the solar desalination industrial. The schematic of supersonic ejector-diffuser system in a solar desalination circulation was illustrated in the Fig. 1. In the solar desalination process, the ejector-diffuser system can be used in reducing the pressure of evaporator and propelling incondensable gas into the condenser. From their experimental and numerical results, the mass flow rate of secondary stream was decreased under the negative influence of guide vanes.

In the present work, a new kind of nozzle with Chevrons was installed inside the supersonic ejector-diffuser system which has been used in the Manohar and Somsak's work [13, 14, 15]. The comparative illustration of supersonic nozzle modification was shown in the Fig.1. New design was based on a convergent nozzle using a new base line to make the position of the Chevrons. Typical Chevron nozzles were illustrated in 3D graphics as showed in the Fig.3. Actually, the nozzle with Chevrons was widely used in the aerospace science and aircraft engine, because it has many advantages such as jet noise reduction, infrared signature control and improvement of conventional converging-diverging nozzle or convergent nozzle [16]. Gregory A. Blaisdell also observes that the nozzle features were improved as a result of installing the Chevrons [17]. In this paper, a numerical method based on Fluent has been applied to simulate supersonic flows and shock waves of the ejector internal flow. Exactly same geometrical model was created to validate the results of experimental data. The Chevron nozzle effects were compared with conventional convergent nozzle refers to the performance of ejector-diffuser system. Optimal Chevrons number was obtained after compare the effects on the ejector-diffuser system.

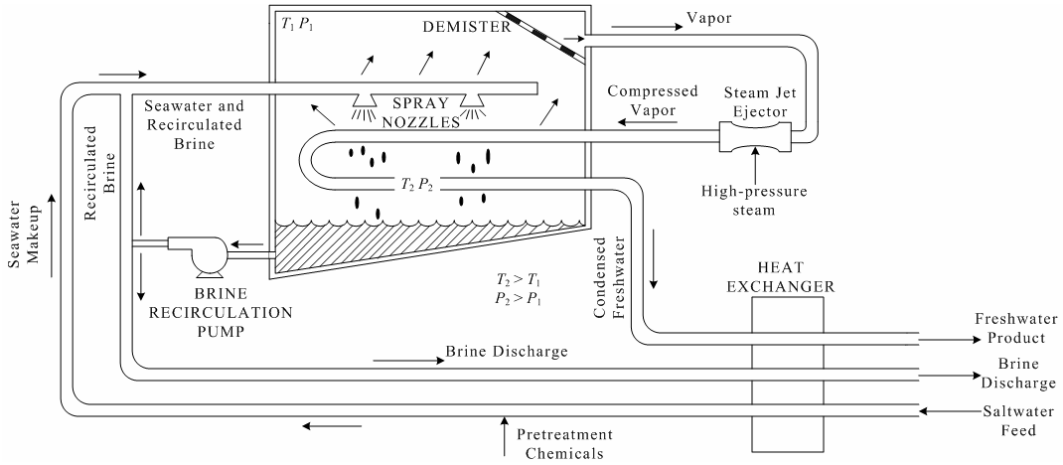

Fig.1 Diagram of a thermal vapor-compression plant (Ref.13)

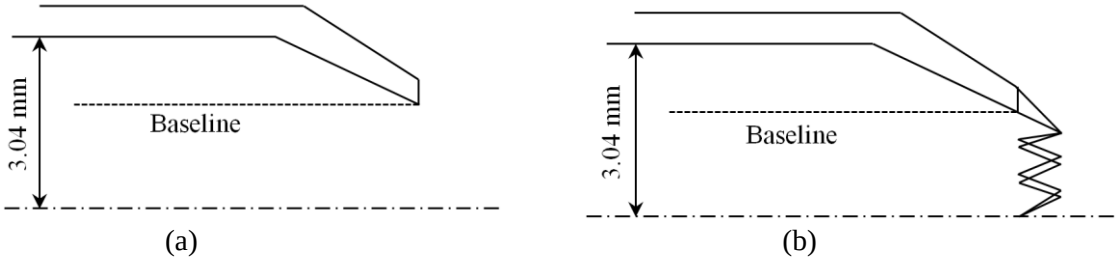

Fig. 2 Comparative illustration of supersonic nozzle modification
(a) Conventional convergent nozzle
(b) Chevron nozzle with same baseline

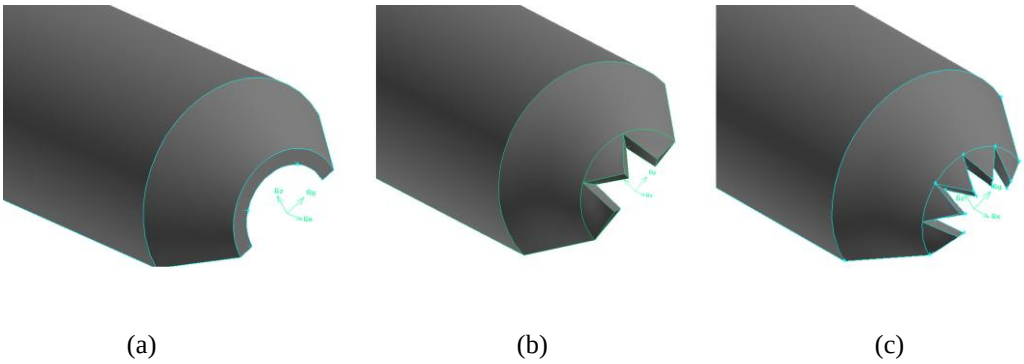

Fig. 3 3D display of the geometrical model of the nozzle
(a) without Chevron (b) with 6 Chevrons (c) 10 Chevrons

2. Numerical Analysis

2.1. Computational Flow Model

As a mixing chamber, two different types were widely used in the solar desalination process: constant mixing chamber area and constant pressure mixing. In this paper, the ejector with a constant mixing area chamber was used, which can be deemed to achieve a higher entrainment ratio [13]. The ejector-diffuser system was shown schematically in the Fig. 4. A three-dimensional symmetric model was applied in the present works. The diameters of supersonic nozzle (D_1), secondary

stream inlet (D_2), mixing section (D_M) and ejector exit (D_E) were kept constant as the values shown in Table 1. At the same time, length of mixing chamber (L_M) and diffuser (L_D) were also fixed.

Fig. 5 represents the half geometrical model of the nozzle with 10 Chevrons. While r represents the radius of the primary inlet tunnel, and r_N is the radius of convergent nozzle and also the base line position of Chevrons. Pointed shape makes the nozzle converge to a radius of r_C. In this figure, 10 Chevrons were distributed averagely outside the previous nozzle exit. For 6 Chevrons, the values of r_C, r and r_N are exactly same to the 10 Chevrons model, only the Chevrons number is different.

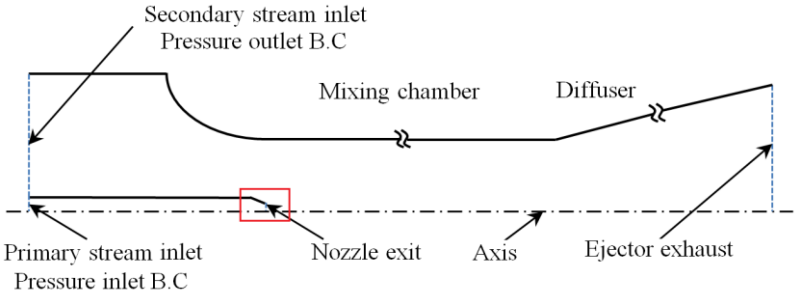

Fig.4 Schematics of the supersonic ejector-diffuser system.

Table 1 Geometrical parameters used in simulations

Ejector-diffuser system		
Diameter of supersonic nozzle	D_1	6.08 mm
Diameter of secondary stream inlet	D_2	34.8 D_1
Diameter of mixing section	D_M	14D_1
Diameter of ejector exit	D_E	34.8 D_1
Length of mixing chamber	L_M	15D_M
Length of diffuser	L_D	12.7D_M

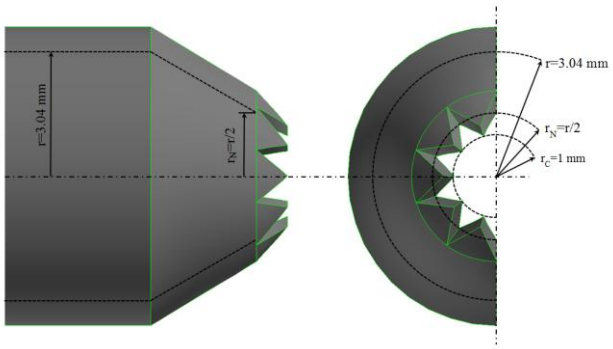

Fig.5 Geometrical model of the nozzle with 10 Chevrons

2.2. Numerical Method

For the CFD software, ANSYS Fluent 14.0 was chosen to simulate internal flows of ejector. Ideal gas was used as the working fluid in all cases. A finite volume scheme and density-based solver with coupled scheme were applied in the computational process. SST k-ω turbulent model, implicit formulations were used considering the accuracy and stability. Second-order upwind scheme was used for turbulent kinetic energy as well as spatial discretizations. Boundary layer effects were considered by making finer grid densely clustered close to the walls. The first (coarse) grid with y+ of about 4.6 has 156,527 cells. The second (medium) grid set has 232,325 cells with a y+ of about 2.7. The third (fine) set grid is generated using the same minimum space as the second set has 345,235 cells. The difference between CFD analysis and experimental results was less than 4%. Hence, the grid independence was also checked. The computational domain with 232,325 cells was chosen because of its less computational time and more accurate result. Pressure inlet boundary condition was set at primary stream inlet of the ejector. The secondary inlet and outlet of ejector were extended to stabilize the computational

results. Pressure outlet boundary conditions with 1 bar were used at both secondary inlet and outlet of the ejector. Therefore, the secondary stream inlet and ejector exit were taken from ambient conditions of an atmospheric pressure.

The total pressure at nozzle exit (P_t) and static pressure (P_s) can be calculated isentropically to give the Mach number. Related initial values can be calculated in these equations:

$$\frac{P_s}{P_t} = \left(1 + \frac{\gamma - 1}{2} M^2\right)^{\frac{-\gamma}{\gamma - 1}} \quad (1)$$

$$\frac{T_s}{T_t} = \left(1 + \frac{\gamma - 1}{2} M^2\right)^{\frac{-\gamma}{\gamma - 1}} \quad (2)$$

Mass flow rate (ṁ) is so important to compare with the experimental data. As one of the indispensable values to describe the ejector-diffuser system performance, the entrainment ratio (Rm) is also obtained from mass flow rate. Entrainment ratio is a ratio between the mass flow rate of secondary flow ($\dot{m}_2$) and primary flow ($\dot{m}_1$). The calculation method of these values can be represented by the following equations:

$$\dot{m} = \rho V A \quad (3)$$

$$Rm = \frac{\dot{m}_2}{\dot{m}_1} \quad (4)$$

Pressure recovery (ΔP) can be defined as the difference between static pressure at the secondary stream inlet (P_{s2}) and static pressure at the outlet of ejector-diffuser system (P_{se}). Sometimes, the pressure recovery coefficient ($\Delta P/P_d$) will be used as a non-dimensional value to describe it.

$$\Delta P = P_{se} - P_{s2} \quad (5)$$

$$\frac{\Delta P}{P_d} = \frac{(P_{se} - P_{s2})}{0.5 \rho V^2} \quad (6)$$

Results and Discussion

3.1. Nozzle flow field comparison

The results from CFD analysis were discussed in detail in this section. Chevrons effects were compared with convergent nozzle based on the data obtained from these figures below. Fig. 6 and 7 present the axial distribution of Mach number and temperature around the nozzle exit extent. With a same primary inlet pressure of about 10bar, the nozzle with Chevrons restricts shock development and makes the shock system weaker after the first big shock. Furthermore, the shock strengthen was decreased under the Chevrons effect. Even though the Chevrons shock strengthen and type are totally different from the convergent nozzle, the nozzle with 10 Chevrons and 6 Chevrons obtain similar results in the axial distribution of Mach number and temperature. Actually, what the first result revealed can be explained as a result of Chevron installation. Under the Chevrons influence, more longitudinal vortices were generated and the nozzle involve more secondary stream into the ejector. The mixing process was enhanced and more energy transfer between two streams would happen. That's why the shock wave became weak compare to the model with convergent nozzle. An interesting phenomenon is the Mach number distribution become smoother after the first strong shock using the Chevron nozzle. More energy was saving and more flows would be entrained.

3.2. Ejector performance

From the previous section, the nozzle effects were discussed in sight of turbulent mixing and compressibility effects. The Chevron effects on ejector performance will be discussed in this section. Fig. 8 and 9 are the ejector performance comparisons between three nozzles, discussed in terms of entrainment ratio and mass flow rate of the nozzle exit. Firstly, the CFD result of convergent nozzle entrainment ratio was compared with experimental data [13] in the Fig.8. According to agreement with experimental results, CFD analysis was validated among these 5 operating conditions.

For the most important coefficient, the entrainment ratio plays a really important role in the performance analysis. Fig. 8 shows that the entrainment ratio was enhanced at least 14.8% under the influence of 10 Chevrons. For 6 Chevrons model, the entrainment ratio was also enhanced, but lowers than the 10 Chevrons model. Better effects on ejector-diffuser were obtained under the Chevrons effects. This analysis was another result of the Chevron effects on internal flow, which has been discussed in 3.1section. Generally speaking, a nozzle with Chevrons can involve more flow vortexes and more vertical flow was introduced into the stream. Therefore, rotary stream passed through the mixing chamber and introduced more shear stress to propel the secondary stream into the ejector-diffuser system, which effectively enhanced the performance of the ejector-diffuser system.

Mass flow rate comparison at nozzle exit using three nozzles was illustrated in the Fig. 9. The mass flow rates of nozzle exit were compared among three nozzles. Under the same pressure condition, the nozzle with Chevrons gets a lower flow at the nozzle exit. That is the result of the installation of Chevrons outside the nozzle, more friction and resistance will be involved. Under the same pressures at the inlet, the effects of the ejector were improved obviously, but the comparisons based on same mass flow rate are also important. Pressure recovery is another indispensable value to study the ejector-diffuser system performance. The pressure recovery comparison between three nozzles was shown in the Fig. 10 with same mass flow rates. From this figure, higher pressure recovery was obtained under the 10 Chevrons effects, which means the secondary stream pressure was elevated to a higher level. The model with 6 Chevrons has no influence on the pressure recovery, and pressure coefficient even decreased at some low mass flow rate cases. Similar analysis can be summarized following the section 3.1 explanation. Under the Chevron nozzle influence, the pressure recovery was increased 8.5% in average, and get a maximum value of 18.9 when it get the mass flow rate of 0.01 kg/s.

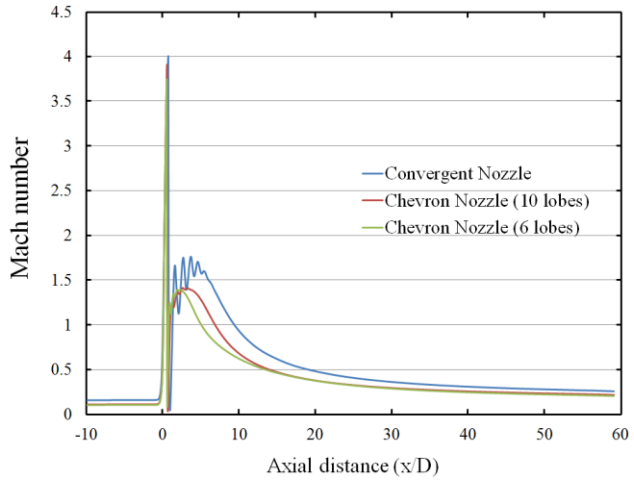

Fig.6 Axial distribution of Mach number under same inlet pressure

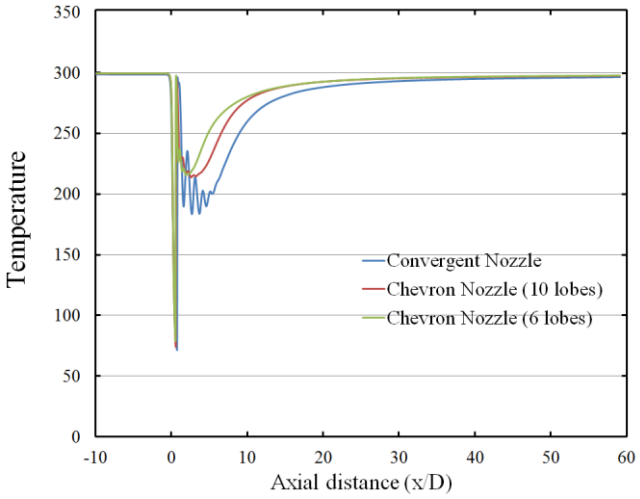

Fig.7 Axial distribution of temperature under same inlet pressure

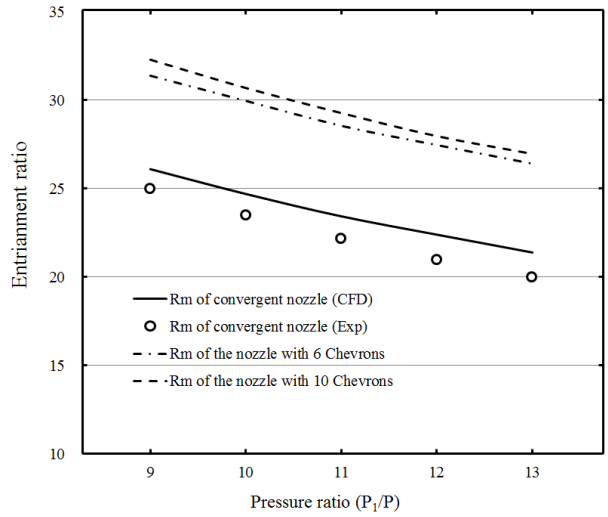

Fig.8 Ejector performance comparison among three nozzles

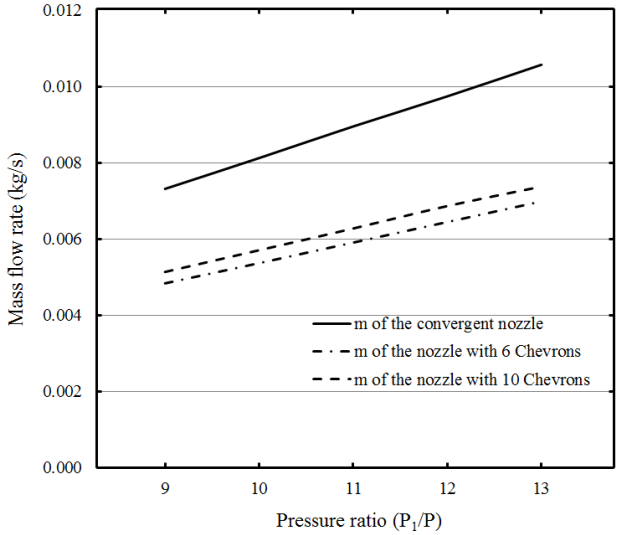

Fig.9 Mass flow rate at nozzle exit using three nozzles

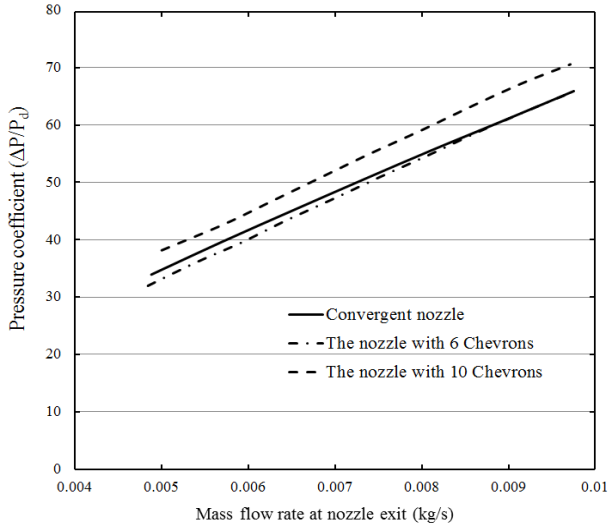

Fig.10 Pressure recovery comparison between three nozzles

Conclusion

In the present paper, a computational method was carried to simulate the internal flow of an ejector-diffuser system. The Chevron nozzle effects on the performance of the ejector were investigated. Numerical results were confirmed by previous experimental data. The numerical simulation results with and without Chevron nozzle have been compared. In the numerical analysis, the Chevron nozzle influence on shock system was obviously obtained. More longitudinal vortices were generated which involved more secondary stream. As the result of the updated model, the model with 10 Chevrons nozzle shows the better results: entrainment ratio was improved 14.8% in average, and the maximum 21.8%. At the same time, pressure recovery was increased 8.5% in average.

Further work is going on to optimize the supersonic ejector-diffuser system with Chevrons.

References

[1] Aidoun Z., Ouzzane M., 2004, "The Effect of Operating Conditions on the Performance of a Supersonic Ejector for Refrigeration," International Journal of Refrigeration, Vol.27, No.8, pp. 974~984.
[2] Bartosiewicz Y., Aidoun Z., Mercadier Y., 2006, "Numerical Assessment of Ejector Operation for Refrigeration Applications Based on CFD," Applied Thermal Engineering, Vol. 26, No. 5-6, pp. 604~612.
[3] J. Yan, S. Shao, J. Liu, Z. Zhang, 2005, "Experiment and Analysis on Performance of Steam-Driven Jet Injector for District Heating System," Applied Thermal Engineering, Vol. 25, No. 8-9, pp. 1153~1167.
[4] K. Chunnanond, S. Aphornratana, 2004, "Ejectors: Applications in Refrigeration Technology," Renewable and Sustainable Energy Reviews, Vol.8, No.2, pp. 129~155.
[5] Y.M. Chen, C.Y. Sun, 1997, "Experimental Study of the Performance Characteristics of a Steam-Ejector Refrigeration System," Experimental Thermal and Fluid Science, Vol. 15, No. 4, pp. 384~394.
[6] B.J. Huang, J.M. Chang, 1999, "Empirical Correlation for Ejector Design," International Journal of Refrigeration, Vol. 22, No. 5, pp. 379~388.
[7] S. Aphornratana, I. W Eames, 1997, "A Small Capacity Steam-Ejector Refrigerator: Experimental Investigation of a System using Ejector with Movable Primary Nozzle," International Journal of Refrigeration, Vol. 20, No. 5, pp. 352~358.
[8] R. Yapıcı, H.K. Ersoy, 2005, "Performance Characteristics of the Ejector Refrigeration System Based on the Constant Area Ejector Flow Model," Energy Conversion and Management, Vol. 46, No. 18-19, pp. 3117~3135.
[9] Y. Bartosiewicza, Z. Aidouna, P. Desevauxb, Y. Mercadierc, 2005, "Numerical and Experimental Investigations on Supersonic Ejectors," International Journal of Heat and Fluid Flow, Vol. 26, No. 1, pp. 56~70.
[10] V. Lijo, H.D. Kim, S. Matsuo, T. Setoguchi, available online 31 August 2011, "A Study of the Supersonic Ejector-Diffuser System with an Inlet Orifice," Aerospace Science and Technology.
[11] M.T. Kandakure, V.G. Gaikar, A.W. Patwardhan, 2005, "Hydrodynamic Aspects of Ejectors," Chemical Engineering Science, Vol. 60, No. 22, pp. 6391-6402.
[12] M.T. Holtzapple, 2001, "High-Efficiency Jet Ejector," Invention Disclosure, Texas A&M University.
[13] D.V. Manohar, 2005, "Desalination of Seawater using a High-Efficiency Jet Ejector," Master Thesis, Texas A&M University.
[14] W. Somsak, 2005, "Optimization of a High-Efficiency Jet Ejector by Computational Fluid Dynamics Software," Master Thesis, Texas A&M University.
[15] W. Somsak, 2008, "CFD Optimization Study of High-Efficiency Jet Ejector," Doctoral Dissertation, Texas A&M University.
[16] Khalid, S., Sokhey, J., Chakka, P., and Pierluissi, A., June 2010, "Ejector/Engine/Nacelle Integration for Increased Thrust minus Drag," 46th AIAA/ASME/SAE/ASEE Joint Propulsion Conference and Exhibit, Nashville, TN, USA, AIAA-2010-6501.
[17] Gregory A. Blaisdell, Anastasios S. Lyrintzis and John P. Sullivan, 2011, "Preliminary Design and Computational Analysis of an Ejector Nozzle with Chevrons" 49th AIAA Aerospace Sciences Meeting including the New Horizons Forum and Aerospace Exposition, Orlando, Florida.

Available online at www.sciencedirect.com

SciVerse ScienceDirect

Procedia Engineering 00 (2012) 000–000

Procedia Engineering

www.elsevier.com/locate/procedia

5th BSME International Conference on Thermal Engineering

A study on aerodynamic drag of a semi-trailer truck

Harun Chowdhury*, Hazim Moria, Abdulkadir Ali, Iftekhar Khan, Firoz Alam and Simon Watkins

School of Aerospace, Mechanical and Manufacturing Engineering, RMIT University, Melbourne, VIC 3083, Australia

Abstract

The primary objective of this study is to determine the aerodynamic impact of various fuel saving devices used in a commercial vehicle (i.e., semi-trailer truck). To measure the aerodynamic drag produced by the vehicle, a wind tunnel study was undertaken using a 1/10th scale model truck. The aerodynamic drags on the baseline vehicle including different external attachments (i.e., front faring, side skirting and gap filling) were measured for a range of vehicle operating speeds and yaw angles, and with different combinations. The results show that these external attachments (fairing and covering) have notable impact on aerodynamic drag as they can reduce up to around 26% aerodynamic drag over the baseline model depending on cross wind effects. The full-skirting (using the front fairing, side skirting and gap filling) has maximum impact whereas only front fairing has minimum impact on aerodynamic drag reduction.

Keywords: Heavy commercial vehicle; aerodynamic drag; fuel saving device; faring; wind tunnel.

Nomenclature

D	aerodynamic drag force (N)
A	projected frontal area (m^2)
C_D	drag coefficient (dimensionless)
V	speed of air (m/s)
ψ	yaw angle (degree)
ρ	air density (kg/m^3)

1. Introduction

Heavy commercial vehicles are considered aerodynamically inefficient compared to other ground vehicles due to their un-streamlined body shapes. A large commercial vehicle travelling at 100 km/h consumes about approximately 52% of the total fuel to provide power to overcome the aerodynamic drag [1]. In contrast, a passenger car under the same driving conditions, consumes approximately 4 times less to overcome drag. Generally, a heavy commercial vehicle's annual mileage can vary between 130,000 km and 160,000 km. Therefore, any reduction of aerodynamic drag will result in huge fuel savings and reduction of greenhouse gas emission. Although a significant effort was made by researchers over the decade to develop various fuel saving devices for commercial vehicles [2], there are still scopes to further reduce the aerodynamic drag.

* Corresponding author. Tel.: +61 3 99256103; fax: +61 3 99256108.
E-mail address: harun.chowdhury@rmit.edu.au

Currently most trucks are equipped with various fuel saving devices or add-ons using aerodynamic shapes in front as well as different parts of the truck to minimize drag. Without out changing the projected frontal area of the truck, it is possible to modify the shapes of the truck including the container box in a more streamlined way. These external attachments can minimize aerodynamic drag based on their external shapes, sizes and placements. Aerodynamic drag (D) depends on the size of a vehicle (projected frontal area, A), the drag coefficient (C_D) which is a measure of the flow quality around the vehicle, and the square of the vehicle speed (V) as expressed in Eq. (1).

$$D = \frac{1}{2} C_D \rho V^2 A \tag{1}$$

where, ρ is the air density. Aerodynamic drag with a semi-trailer truck typically accounts for about 75-80% of the total resistance to motion at 100 km/h [3]. Therefore, reducing aerodynamic drag contributes significantly to the fuel economy of a truck as well as the reduction of green house gas emissions [4-6]. For this reason, drag remains the focal point of vehicle aerodynamics. The aerodynamic effects on current designs of aerodynamic fairings (front and side) and their combinations were not well studied and documented. As the number of trucks have been increased significantly worldwide due to increased logistic transportations, it is utmost important to study the effectiveness of fuel saving devices on existing trucks in order to minimize aerodynamic drag. Limited research has been undertaken in this regard. Therefore, the primary objective of this work is to investigate the possibilities for further reduction of aerodynamic drag using aerodynamic fairings with various combinations in order to increase its effectiveness.

2. Experimental methods

The RMIT Wind Tunnel was used to measure the aerodynamic drag on the experimental model. The maximum speed of the tunnel is approximately 145 km/h. Details of this tunnel can be found in [7]. In order to keep the airflow around the test vehicle as practical as possible, a 10% scale model of a semi-trailer truck was used. The experimental truck model was connected through a mounting strut (see Fig. 1) with the JR3 multi-axis load cell, also commonly known as a 6 degree of freedom force-torque sensor made by JR3, Inc., Woodland, USA. The sensor was used to measure all three forces (drag, lift and side forces) and three moments (yaw, pitch and roll) at a time. Each set of data was recorded for 10 seconds time average with a frequency of 20 Hz ensuring electrical interference is minimized. Multiple data sets were collected at each speed tested and the results were averaged for minimizing the further possible errors in the raw experimental data.

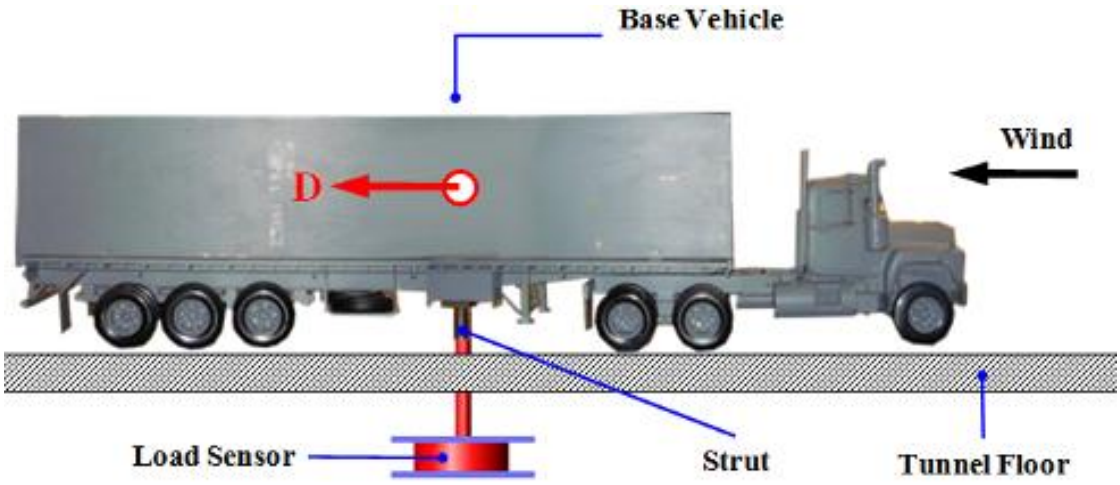

Fig. 1. Schematic of the experimental setup.

All three forces (drag, lift and side force) and their corresponding moments were measured. Tests were conducted at a range of wind speeds (40 km/h to 120 km/h with an increment of 10 km/h) under four yaw angles (0º, 5º, 10º and 15º) to simulate the crosswind effects. Yaw angle (ψ) can be defined as the angle between the vehicle centerline and the mean direction of airflow experienced by the vehicle as indicated in Fig. 2. Various fuel saving devices (front and side faring) were designed and manufactured for attaching on the base truck model. These add-ons were 10% scale of their full-size to

match the scale model. Fig. 3 shows different add-ons used in this study. In this paper, only drag force (D) data and its dimensionless parameter drag coefficient (C_D) are presented. The C_D was calculated by using the following formula:

$$C_D = \frac{D}{\frac{1}{2}\rho V^2 A} \tag{2}$$

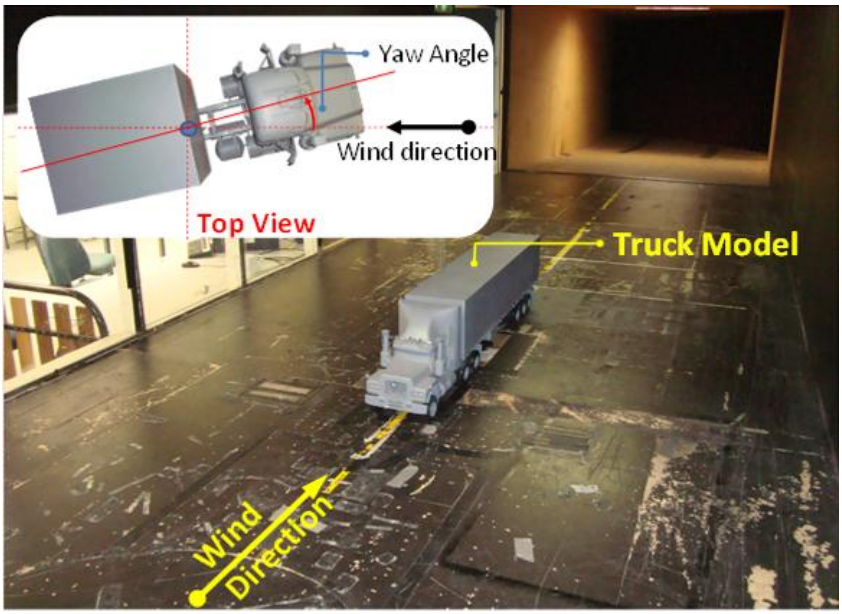

Fig. 2. Experimental arrangement in the test section of RMIT Wind Tunnel.

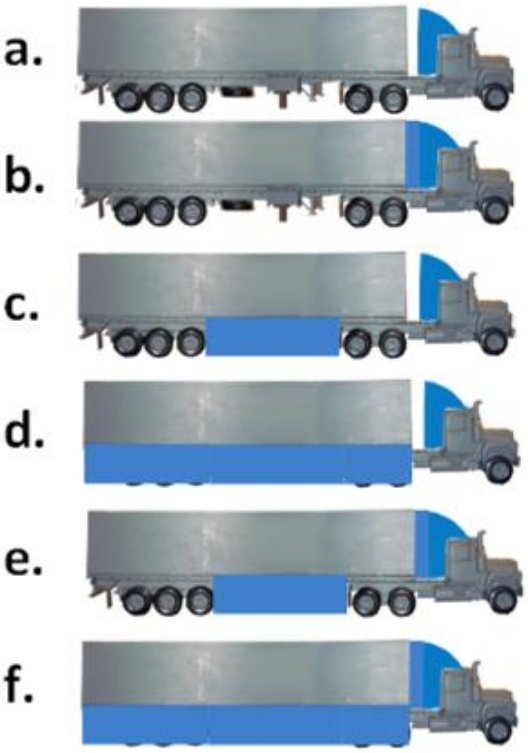

Fig. 3. Different combinations of fairing on the baseline semi-trailer truck model.

3. Results

The C_D as a function of speed for various configurations of fairing at 0º yaw angle is presented in Fig. 4. The figure shows that the baseline model has almost constant C_D value about 0.8. Similar results were found by Watkins et al. [8]. Generally, C_D values for a semi-trailer truck are ranges from 0.5 to 0.9 depending on the aerodynamic design of the truck. The baseline model has the highest C_D value whereas the model with any fairing attached has lower C_D values. Experimental data also indicate a decrease of C_D values with the increase of speed for the baseline model with any fairing attachment. The baseline model with the front and side fairing, and gap filled (i.e., *configuration–a*) as shown in Fig. 3 has the minimum C_D value among all other configurations tested.

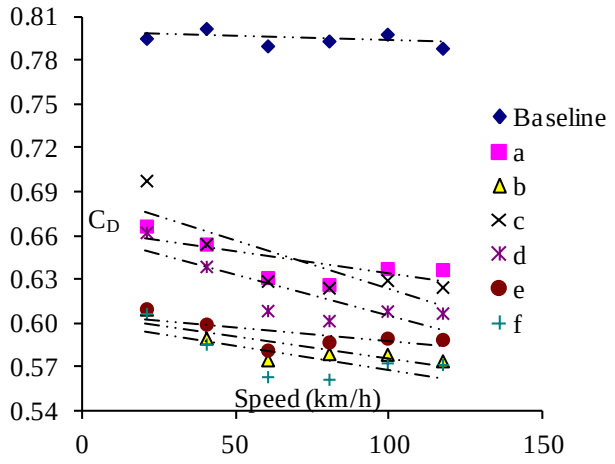

Fig. 4. Drag coefficient as a function of speed for different test configurations at ψ = 0º base line.

As mentioned earlier that the base vehicle model has also been tested alone with all attachments with different combinations at other yaw angles (ψ = 5º, 10º and 15º) to study the cross wind effect. The percentage of aerodynamic drag decrease over the base vehicle is shown in Fig. 5 for four yaw angles (ψ = 0º, 5º, 10º and 15º).

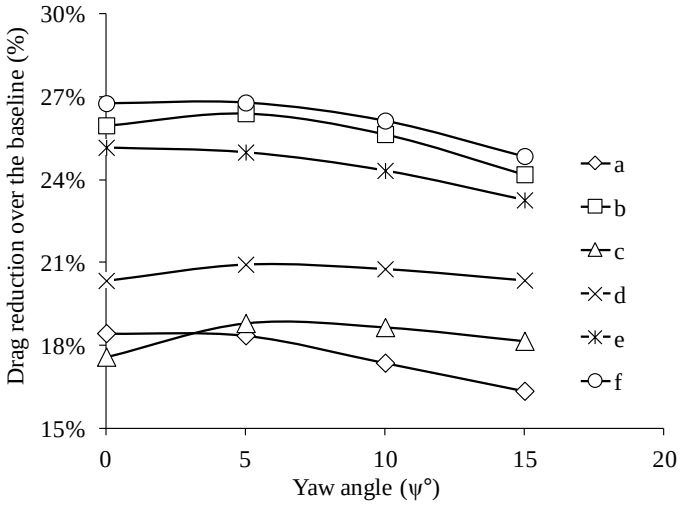

Fig. 5. Drag increase over base vehicle in percentage as a function of yaw angle.

The yaw angles have different effects on different combinations on the baseline model. For example, aerodynamic drag decreases with the increase of yaw angles for *configuration a*, *e* and *f*. However, the drag increases with the increase of yaw angle up to 5º and thereafter drag decrease with further increase of yaw angle for *configurations b*, *c* and *d*. Table 1 represents the percentage reduction of average drag over the baseline on yaw angle variation from 0º to 15º. The results show that the about 17.6% drag decreased with the "*configuration a*" and about 26.1% drag reduction with "*configuration - f*".

Table 1. Percentage reduction of drag (*D*) on yaw angle variation from 0º to 15º over the baseline.

Configuration	Average drag reduction
a	17.6%
b	25.5%
c	18.3%
d	20.6%
e	24.4%
f	26.1%

4. Discussion

There are two main parts of a semi-trailer truck: a tractor unit (consists of engine compartment, cabin, sleeper, fuel tanks, air drams and axels) and a detachable semi-trailer unit. Several gaps can be found in a semi-trailer truck. For example, gaps between the semi-trailer and the tractor unit. Additionally, several open spaces can be found near the lower section of the semi-trailer unit. Wheels are also kept uncovered. The experimental data indicated that not only by using the front fairing but also by covering different parts of the gaps in different portion has effect on aerodynamic drag reduction. It is clear that the amount of area covered by the external fairing plays important role for the reduction of drag. Results indicated that partial covering of the gaps can enhance the performance for drag reduction whereas full covering indicated the maximum drag reduction. Thus, it is possible to reduce drug as well as fuel consumption by using external attachments by covering the gaps and open area within the tractor and the semi-trailer unit. Fixed or detachable covering can be used to cover the open area on both sides of the semi-trailer near the bottom part including the wheels. However, flexible covering can be used to cover the gap between the tractor and the semi-trailer units as the gap can vary during turning the vehicle.

5. Conclusions

The aerodynamic fairings have notable impact on aerodynamic drag. The front fairing alone can reduce around 17% of drag. Further drag reduction up to 26% is possible using various combinations of aerodynamic fairings in different parts of the truck body. The baseline model with the front fairing and side covering including filling the gap between the truck and container box exhibits maximum drag reduction among all configurations tested. Thus, the semi-trailer truck with maximum amount of surface area covered can enhance the drag reduction performance.

References

[1] Schoon, R. E., 2007. On-road Evaluation of Devices to Reduce Heavy Truck Aerodynamic Drag. SAE Publication, SAE Paper No. 2007-01-4294.
[2] Cooper, K. R., 2006. Full-Scale Wind Tunnel Tests of Production and Prototype, Second-Generation Aerodynamic Drag-Reducing Devices for Tractor-Trailers. SAE Publication, SAE Paper No. 2006-01-3456.
[3] Hucho, W. H., 1998. Aerodynamics of Road Vehicles, 4th ed., Society of Automotive Engineers (SAE),Warrendale.
[4] Snyder, R. H., 1997. Tire Rolling Losses and Fuel Economy. SAE Special Publication, SAE Paper No.74.
[5] Landman, D., Wood, R. M., Seay, W. S., 2009. Understanding Practical Heavy Truck Drag Reduction Limits. SAE Publication, SAE Paper No. 2009-01-2890.
[6] Schoon, R. E., 2007. On-road Evaluation of Devices to Reduce Heavy Truck Aerodynamic Drag. SAE Publication, SAE Paper No. 2007-01-4294.
[7] Alam, F., Chowdhury, H., Moria, H., Watkins, S., 2010. Effects of Vehicle Add-Ons on Aerodynamic Performance, in "*The Proceeding of the 13th Asian Congress of Fluid Mechanics (ACFM2010)*". Bangladesh University of Engineering and Technology, Dhaka, p.186.
[8] Watkins, S., Saunders, J. W., Hoffmann, P. H., 1987. Wind Tunnel Modelling of Commercial Vehicle Drag Reducing Devices: Three Case Studies. SAE Publication, SAE Paper No. 870717.

Available online at www.sciencedirect.com

SciVerse ScienceDirect

Procedia Engineering 00 (2012) 000–000

Procedia Engineering

www.elsevier.com/locate/procedia

5th BSME International Conference on Thermal Engineering

Biomechanical Analysis of Foot Pressures during Walking

Md. Tofajjal Hossain Chowdhury[a], Yong-Jin Kim[b], a*

[a]*Department of Mechanical Engineering, Bangladesh University of Engineering & Technology (BUET), Dhaka-1000, Bangladesh*
[b]*Division of Mechanical and Automotive Engineering, College of Engineering, Kongju National University, 275 Boodae-Dong, Cheonan, Chungnam-do, South Korea*

Abstract

The experimental investigation was in designing a shoe insole by measuring the peak pressures and center of pressure (COP) under the feet while walking with shoes on. Four subjects (two men and two women) participated in this study. The pressure data was obtained by using footscan® insole technology (RSscan International, Olen, Belgium). Pressure-time relationship and COP were found to be important factors influencing foot stability. The pressure distribution and COP patterns during walking were similar in both feet for all subjects. During walking, the peak pressures in both feet for all subjects were under the heel and metatarsal head, followed by the big toe. This study shows that the design for the left and right insole should be the same for walking purposes. The insoles should be designed in consideration of the peak pressures on the heel, metatarsal head and big toe regions during walking. The insole design suggested in this study is recommended for reducing foot-pressure and for providing comfort during walking.

Keywords: Foot-Pressure; COP; Biomechanics; Insole Technology

1. Introduction

According to previous research done by Jorgensen and Ekstrand, 1988, Chen et al., 1994, Kogler et al., 1996, Hodge et al., 1999, a variety of foot inserts or foot orthoses designs demonstrate different kinetic modifications and show the changes of foot pressure distribution as well as the reduction of pressure, impact force, and perceived comfort and they also showed that use of a heel pad, arch support, metatarsal pad and total contact insert (TCI) do the same [1-4]. Light et al., 1980, explained that a heel pad is effective in reducing the strike impact and pressure on the heel [5]. Lee et al., 2004, found that a metatarsal pad reduced forefoot pressure and transferred weight bearing to the longitudinal and metatarsal arches [6]. Lord and Hosein, 1994 and Chen et al., 2003, showed that a total contact insert (TCI) provided pressure relief in the heel and forefoot regions [7-8]. Lee and Hong, 2005, examined the changes in foot pressure distribution, impact force, and perceived comfort using a heel cup, arch support, metatarsal pad, and the TCI in case of high heeled shoes [9]. Since motion in various parts of the body triggers reactive forces from the shoe-ground contact, according to Mann, 1991, and Schneck and Bronzino, 2004, a study of this interaction is an excellent opportunity to analyze the biomechanical conditions prevailing during walking [10-11]. It was found that the walking motions of both feet are symmetrical and the pressure distribution between them is similar. The present study examined the peak pressures and the COP on the feet during walking in order to suggest comfortable insole designs.

* Corresponding author. Tel.: +8801683770779, +8801674173693.
E-mail address: rashed9837@yahoo.com, rashed9837@hotmail.com

2. Experimental Procedure

2.1. Subjects

Four subjects (two men and two women) took part in this study. None of the participants had any deformities. Table 1 shows the subjects' characteristics.

Table 1. Subjects characteristics: age, body weight, and height

Subjects	Age (yrs)	Body weight (kg)	Height (m)
Man (1)	22	68	1.76
Man (2)	31	63	1.73
Woman (1)	21	71	1.75
Woman (2)	21	55	1.65

2.2. Instrumentation and Data collection

Cordero et al., 2004 and Han et al., 1999 used the insole system to calculate complete ground reaction force and COP respectively [12-13]. In this experiment, the footscan® insole technology (Rsscan International, Olen, Belgium, 500Hz) was to measure vertical ground reaction force (GRF), which was then used to calculate in-shoe pressures and COP. The experimental setup is illustrated in figure 1. Both insoles were connected to a data logger attached to the waist of the subject (fig. 1). Data was stored on a memory card (4Mb) using a cordless remote control device. Data for 8s of walking was recorded, but it took 0.7-0.85s to analyze each step. The measurements along with the subject's body weights were immediately checked using footscan® insole software 2.39.

(a) (b) (c)

Fig. 1. (a) The experimental setup: rsscan insoles, data logger with remote control, the footscan® insole technology; (b) Experimental data collection during walking; (c) The 2D foot screen represents eighteen anatomical landmarks.

2.3. Data analysis

In insole technology, landmarks (T1-T5, M1-M5, V1-V4, H1-H4: fig. 1) are located on the pressure images, which are based on the anatomical structures of the foot (Appendix A). According to De Cock et al., 2005, and Willems et al., 2005, ten (T1, M1-M5, H1-H4: fig. 1) out of the eighteen anatomical landmarks were considered based on pressure distribution criteria during walking [14-15]. This study showed that the vertical ground reaction force (GRF)-time curves (fig. 2) for all subjects were similar to Lee and Hong's curve in 2005 [9].

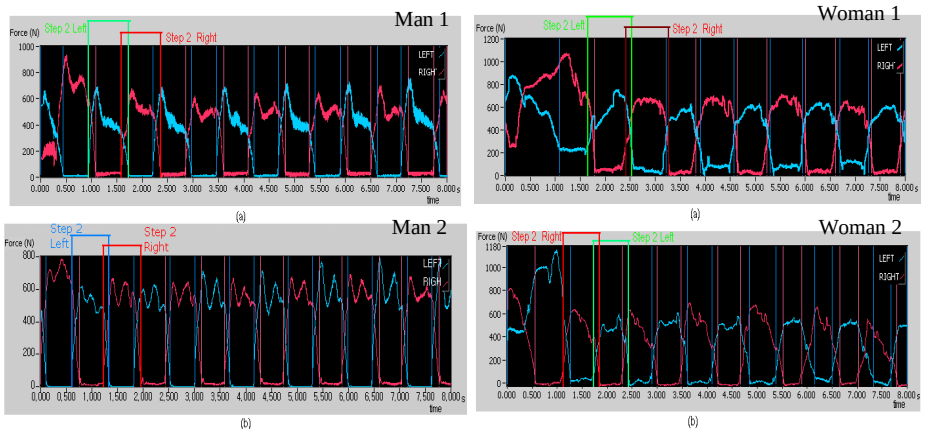

Fig. 2. Vertical GRF (N)-time (s) curves under both feet during walking: (a) men 1 & 2; (b) women 1 & 2.

3. Results

3.1. Pressure and Peak pressure effects during walking

In figure 3 (0-780 ms: man 1, 0-750 ms: man 2, 0-850 ms: woman 1, and 0-700 ms: woman 2), the patterns of pressure under heel (H1-H4), metatarsal heads (M1-M5), and toes (T1-T5) are similar. The pressure increases under the heel (H1-H4), the metatarsal heads (M1-M5), and the toes (T1-T5) respectively for all subjects. Moreover, the peak pressure (fig. 4) is changing in a decreasing order in the regions of the H1, H2, M1, H3, M2, H4, M3, M4, T1, and M5 during walking for all subjects.

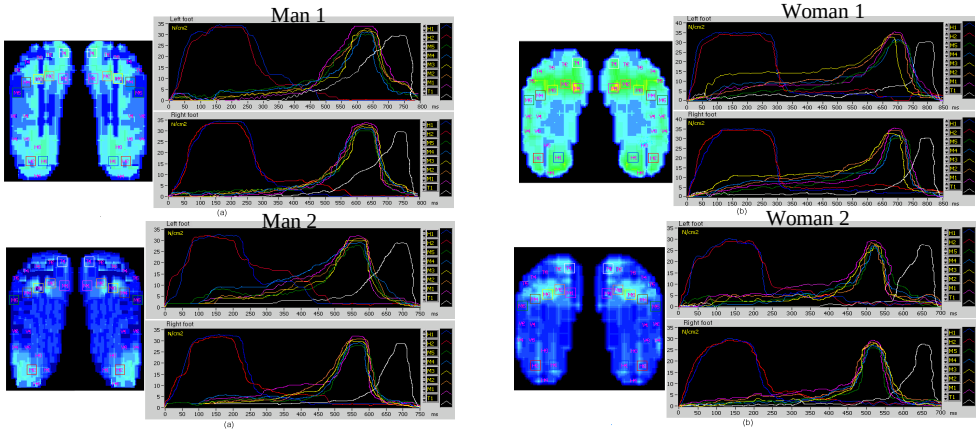

Fig. 3. The pressure screen (2D views) and pressure (N/cm2)-time (ms) curves over eight landmarks :(a) men 1 & 2; (b) women 1 & 2.

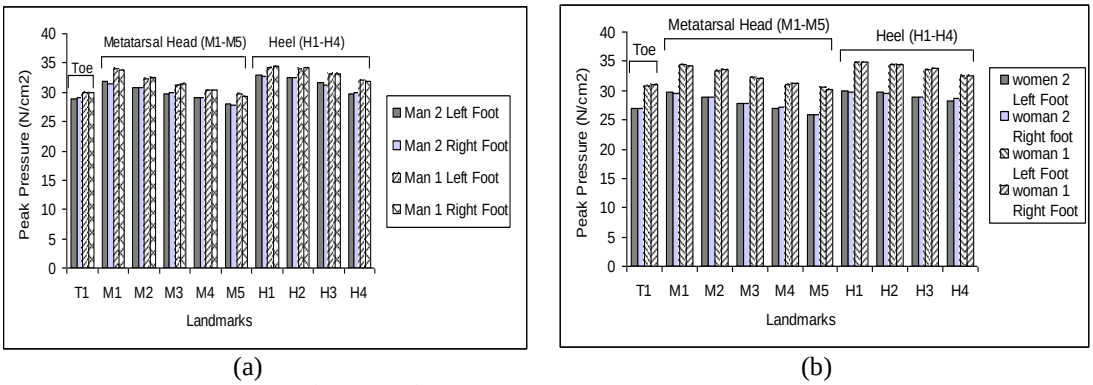

Fig. 4. Peak pressures under left and right foot over ten landmarks during walking: (a) men 1 & 2; (b) women 1 & 2.

3.2. COP effect during walking

In figure 5, the patterns of the COP are found to be the same during walking for all subjects. It is observed that there is a cyclic and symmetric movement between the two feet for all subjects. Besides, COPx (medial-lateral) and COPy (anterior-posterior) are also observed to be similar in both feet for all subjects. Figure 5 shows that during walking, the overall COPx and COPy for woman 1 are higher than those for man 1, man 2, and woman 2 respectively; this difference can be explained by the differing body weights of the subjects.

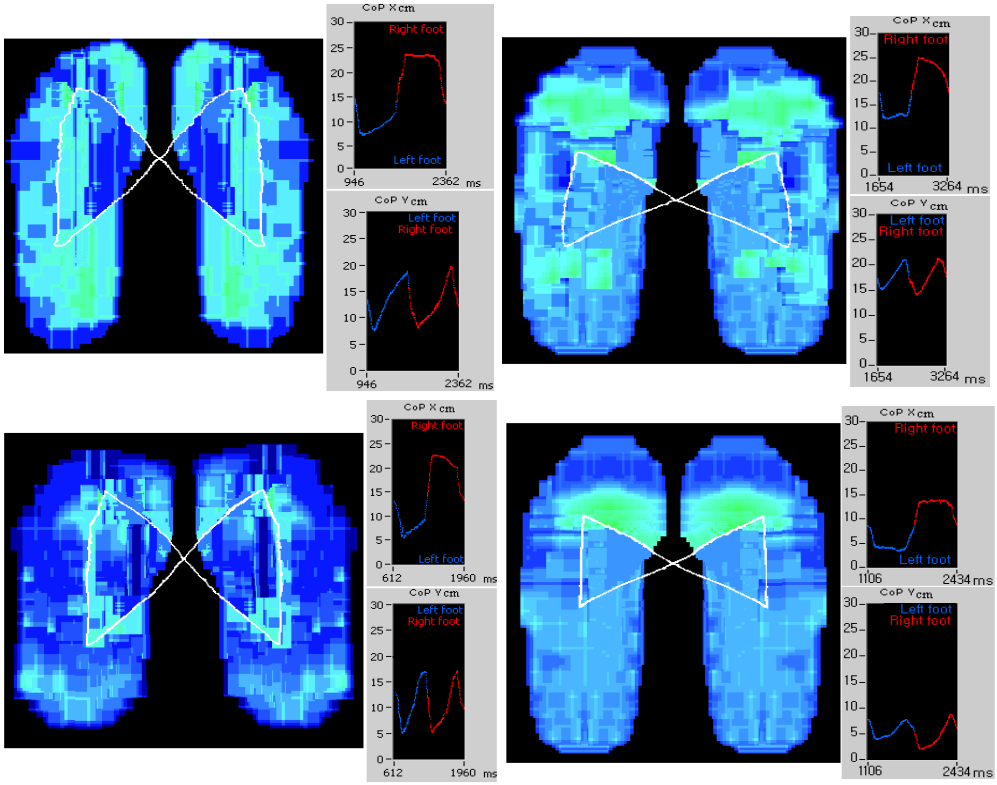

(a) (b)

Fig. 5. The COP screen (2D views) and COPx (cm)-time (ms) as well as COPy (cm)-time curves during walking (step 2): (a) men 1 & 2; (b) women 1 & 2.

4. Discussion

4.1. Comparison between the subjects during walking

The supplied graphs (fig. 3 & fig. 5) indicate that the pressure distribution is the same in both feet and the COP is symmetric between them as well. COPx (medio-lateral) and COPy (antero-posterior) were used as an indicator of stability by Hof et al., 2005 and Prieto et al., 1996 [16-17]. The overall stability or instability (fig. 5) is the same in both feet during walking. It can be seen from figure 3 that the pressure distribution and the patterns of pressure under the left and right feet are almost the same during walking. A small difference is found in the magnitudes (fig. 4) of peak pressure over selected landmarks between the subjects.

4.2. Design suggestion for insoles

According to Abboud and Rowley, 1996, foot-pressure measurements are of the utmost importance in understanding the central role of biomechanical issues during walking [18]. The heel (H1, H2, H3, and H4), the metatarsal heads (M1, M2, M3, M4, and M5) and the big toe (T1) regions of the insole should be designed with respect to the peak pressure and the COP. This means the insoles should be designed in the medial-lateral side in the anterior-posterior direction and also that the insole designs would be the same for the left and right feet.

According to these criteria, the insole design presented in Appendix A may be suitable for comfortable walking. It may be a good attempt to make a design according to the biomechanical and biodynamic requirements of the subjects.

5. Conclusion

The results imply similar pressure characteristics for the left and right feet due to the symmetric movement of the two feet during walking. The present study shows that the same design should be considered for both feet. The design of big toe, metatarsal heads, and heel regions of the insole should be based on the peak pressures and COP data. Thus, this insole design is optimum for enhancing stability and comfort during walking since it greatly reduces peak pressure and COP on the feet.

6. Further Recommendation

The following recommendations would be suitable for future work:

i. Insoles should be designed in accordance to the data on peak pressures. The locations of the landmarks in the insoles should be determined with respect to the walking results for all subjects.
ii. After making the insoles, the pressure data should be taken again using the footscan® insole technology. It is recommended to compare the peak pressure results under the selected modified regions with the previous results.

Acknowledgements

This study was supported by LESTE Company, Ltd., 503 Research Building, 182 Shinkwan-Dong, Gongju-si, Chungnam-do, 314-701, South Korea.

References

[1] Jorgensen, U., Ekstrand, J., 1988. Significance of Heel Pad Confinement for the Shock Absorption at Heel Strike. International Journal of Sports Medicine 9, p. 468.
[2] Chen, H., Nigg, B.M., De Koning, J., 1994. Relationship between Plantar Pressure Distribution under the Foot and Insole Comfort. Clinical Biomechanics 9, p. 335.
[3] Kogler, G.F., Solomonidis, S.E., Paul, J.P., 1996. Biomechanics of Longitudinal Arch Support Mechanisms in Foot Orthoses and their Effect on Plantar Aponeurosis Strain. Clinical Biomechanics 11, p. 243.
[4] Hodge, M.C., Bach, T.M., Carter, G.M., 1999. Orthotic Management of Plantar Pressure and Pain in Rheumatoid Arthritis. Clinical Biomechanics 14, p. 567.
[5] Light, L.H., Mclellan, G.E., Klenerman, L., 1980. Skeletal Transients on Heel Strike in Normal Walking with Different Footwear. Journal of Biomechanics 13, p. 477.
[6] Lee, G.H., Han, S.J., Lee, S.G., Park, S.B., 2004. The Effect of Metatarsal Pad for Foot Pressure. Journal of Korean Academy of Rehabilitation Medicine 28, p. 94.
[7] Lord, M., Hosein, R., 1994. Pressure Redistribution by Molded Inserts in Diabetic Footwear: A Pilot Study. Journal of Rehabilitation Research Division 31, p. 214.
[8] Chen, W.P., Ju, C.W., Tang, F.T., 2003. Effect of Total Contact Insoles on the Plantar Stress Redistribution: A Finite Element Analysis. Clinical Biomechanics 18, p. 17.
[9] Lee, Y.H., Hong, W.H., 2005. Effects of Shoe Inserts and Heel Height on Foot Pressure, Impact Force, and Perceived Comfort during Walking. Applied Ergonomics 36, p. 355.
[10] Mann, R.A., 1991. Overview of Foot and Ankle Biomechanics, Chapter 14 in "Disorders of the Foot & Ankle: Medical and Surgical Management" M.H. Jahss, Editor. WB Saunders Company, London, U.K., p. 385.
[11] Schneck, D.J., Bronzino, J.D., 2004. Biomechanics: Principles and Applications. Journal of Biomechanics 37, p. 169.
[12] Cordero, A.F., Koopman, H.J.F.M., Helm, F.C.T., vander, 2004. Use of Pressure Insoles to Calculate the Complete Ground Reaction Forces. Journal of Biomechanics 37, p. 1427.
[13] Han, T.R., Paik, N.J., Im, M.S., 1999. Quantification of the Path of Center of Pressure (COP) using An F-scan In-shoe Transducer. Gait & Posture 10, p. 248.
[14] De Cock, A., De Clercq, D., Willems, T.M., Witvrouw, E., 2005. Temporal Characteristics of Foot Rollover during Barefoot Jogging: Reference Data for Young Adults. Gait & Posture 21, p. 432.
[15] Willems, T.M., Witvrouw, E., Delbaere, K., De Cock, A., De Clercq, D., 2005. Relationship between Gait Biomechanics and Inversion Sprains: A Prospective Study of Risk Factors. Gait & Posture 21, p. 379.
[16] Hof, A.L., Gazendam, M.G.J., Sinke, W.E., 2005. The Condition for Dynamic Stability. Journal of Biomechanics 38, p. 1.
[17] Prieto, T.E., Myklebust, J.B., Hoffmann, R.G., Lovett, E.G., Myklebust, 1996. Measures of Postural Steadiness: Differences between Healthy Young and Elderly Adults. IEEE Transactions on Biomedical Engineering 43, p. 956.
[18] Abboud, R.J., Rowley, D.I., 1996. Foot Pressure Measurement-History and Development, 4th Ed. Chapter 3 in "Surgery of Disorders of Foot and Ankle". Martin Dunitz. Ltd, p. 123.

Appendix A. Anatomy of the foot and Design of the insoles for shoe

A.1. Anatomy of the foot

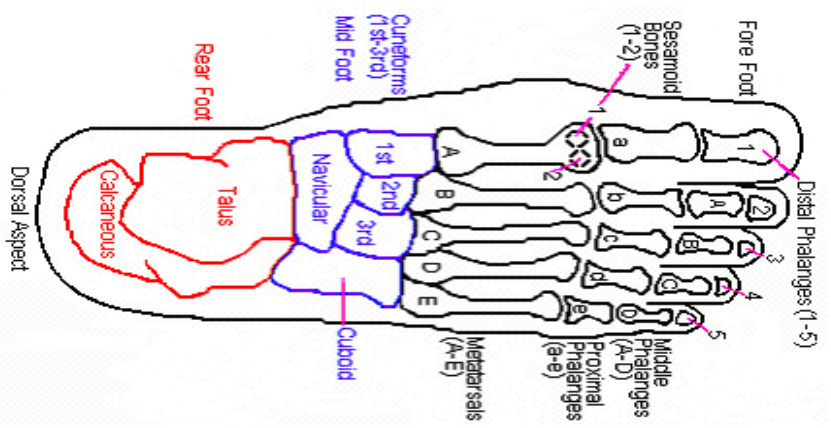

Fig. A.1. Bone structure of the human foot.

A.2. Design of the insoles for shoe

The insoles should be designed under the big toe (T1), metatarsal heads (M1-M5), and heel (H1-H4) based on peak pressures during walking for all subjects.

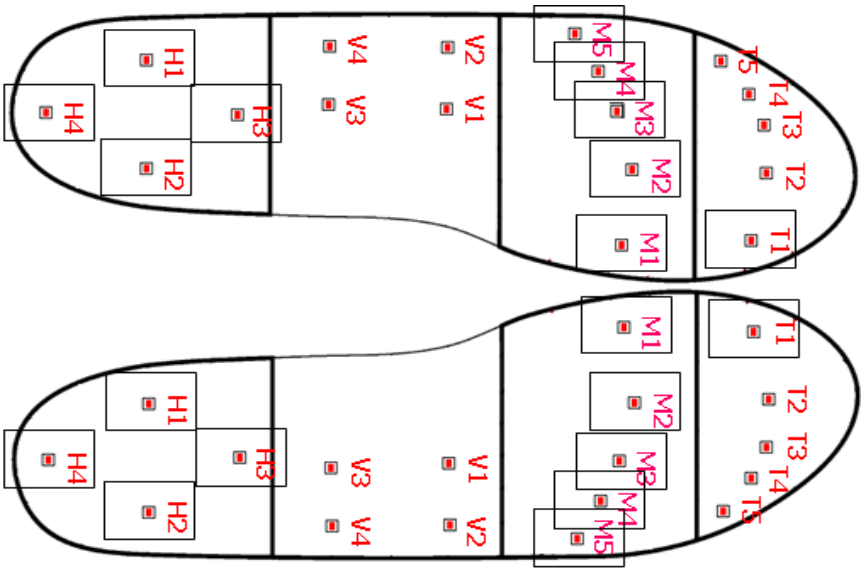

Fig. A.2. The suitable design of the insoles for shoe.